



HAL
open science

Trace element partitioning between clinopyroxene and alkaline magmas: parametrization and role of M1 site on HREE enrichment in clinopyroxenes

Céline Baudouin, Lyderic France, Marine Boulanger, Célia Dalou, Jean-Luc Devidal

► To cite this version:

Céline Baudouin, Lyderic France, Marine Boulanger, Célia Dalou, Jean-Luc Devidal. Trace element partitioning between clinopyroxene and alkaline magmas: parametrization and role of M1 site on HREE enrichment in clinopyroxenes. *Contributions to Mineralogy and Petrology*, 2020, 175 (5), 10.1007/s00410-020-01680-6 . hal-02629068

HAL Id: hal-02629068

<https://hal.science/hal-02629068>

Submitted on 28 Sep 2020

HAL is a multi-disciplinary open access archive for the deposit and dissemination of scientific research documents, whether they are published or not. The documents may come from teaching and research institutions in France or abroad, or from public or private research centers.

L'archive ouverte pluridisciplinaire **HAL**, est destinée au dépôt et à la diffusion de documents scientifiques de niveau recherche, publiés ou non, émanant des établissements d'enseignement et de recherche français ou étrangers, des laboratoires publics ou privés.

1 **Accepted 31 March 2020**

2 **Trace element partitioning between clinopyroxene and alkaline magmas:**
3 **parametrization and role of M1 site on HREE enrichment in**
4 **clinopyroxenes.**

5

6

7 Céline Baudouin¹, Lydéric France¹, Marine Boulanger¹, Célia Dalou¹, Jean-Luc Devidal²

8

9

10 ¹Université de Lorraine, CNRS, CRPG, F-54000 Nancy, France

11 ²Laboratoire Magmas et Volcans, Université Clermont Auvergne, CNRS, IRD, OPGC, 63178
12 Aubière, France

13

14

15

16

17

18

19

20

21

22 ***Corresponding author: Céline Baudouin**

23 **E-mail: baudouin.geol@gmail.com**

24

25

26 **Abstract**

27

28 Trace element partitioning between minerals and liquids provides crucial constraints
29 on igneous processes. We quantified trace element concentrations in clinopyroxene (Cpx)
30 phenocrysts and their phonolite melt inclusions from the 2007-08 eruption of Oldoinyo
31 Lengai (Tanzania), and report Cpx-melt partition coefficients (D) and corresponding
32 partitioning equations for rare earth elements (REE) and high field strength elements (HFSE)
33 in alkaline magmas. Heavy REE (HREE: Er, Tm, Yb, Lu) are enriched relative to middle
34 REE in alkaline Cpx and display a specific partitioning behavior that is characteristic of
35 alkaline systems. HFSE (Ti, Zr, Hf) and HREE have similar D values ($D_{\text{Hf}} = 0.25$; $D_{\text{Lu}} = 0.4$)
36 that are significantly higher than MREE ($D_{\text{Sm}} = 0.06$). High $D_{\text{HREE}}/D_{\text{MREE}}$ are strongly
37 correlated with the high values of D_{Zr} and D_{Hf} relative to the low D_{MREE} values. In this study,
38 REE partitioning between phonolite melt and Cpx is not consistent with standard models
39 assuming incorporation of all REE in the Cpx M2 site, but rather highlights HREE
40 substitution in both the M1 and M2 sites. Here we highlight the preferential incorporation of
41 HREE in the VI-coordinated M1 site, whereas light REE and MREE remain mostly
42 distributed in the VIII-coordinated M2 site. REE partitioning is strongly dependant on Cpx
43 chemistry: the ideal ionic radius and HREE incorporation in the M1 site increase with
44 increasing Fe^{3+} content and decrease with increasing Mg^{2+} and Al^{VI} content. In our study, we
45 focus on alkaline evolved magmas, and update existing models to obtain adequate D_{HREE} for
46 alkaline evolved melts. We provide equations to quantify REE and HFSE partitioning, and
47 HREE enrichment in Cpx, those are based on Cpx major element composition and
48 temperature. We propose a new model based on the lattice strain approach that predicts HREE
49 partitioning between Cpx and alkaline magmas. The knowledge of the melt composition or of
50 the trace element contents is not required to obtain D_{REE} from the new model. An improved
51 parameterization of HFSE partitioning between Cpx and phonolite and trachy-phonolite melts
52 is also provided herein. We eventually discuss the potential implications of those new data on
53 our understanding of REE deposits that are commonly associated with igneous alkaline
54 complexes.

55

56 **Keywords:** partition coefficient; clinopyroxene; HREE enrichment; M1 site; alkaline magmas;
57 REE deposits

58

59 Introduction

60

61 The trace element contents of minerals and melts are used to identify and quantify
62 igneous processes such as partial melting, equilibrium or fractional crystallization, and
63 melt/rock interactions. Those processes are responsible for local economic concentrations of
64 various metals (e.g., rare earth elements, REE), especially in the case of alkaline igneous
65 provinces, which not only feed some of the most famous volcanoes worldwide (e.g.,
66 Vesuvius, Etna, Oldoinyo Lengai, Erebus), but are also associated with numerous critical
67 metal deposits (e.g., Mountain Pass, USA; Ilmaussaq, Greenland). The partitioning of key
68 trace elements (Nb, Ta, REE) along the liquid line of descent and their corresponding
69 enrichment in mineral phases are governed by the amount and chemistry of fractionating
70 minerals, and by the chemistry of the corresponding melts. The partition coefficient quantifies
71 the distribution of a given element i between a mineral and a melt ($D_i^{\text{mineral/melt}} = \frac{C_i^{\text{mineral}}}{C_i^{\text{melt}}}$).
72 In the case of alkaline magmas, few partitioning data are available for the various crystallizing
73 minerals (Mollo et al. 2016, 2018; Olin and Wolff 2010; Baudouin & France 2019; Beard et
74 al. 2019).

75 Clinopyroxene (Cpx) is a widespread mineral in igneous rocks, and has a major
76 impact on the liquid line of descent of the corresponding magmas. In alkaline silicate igneous
77 rocks (syenite, phonolite, nephelinite) and carbonatites (the main REE deposits on Earth), Cpx
78 commonly displays sinusoidal REE patterns with peculiar and unexpected heavy REE
79 (HREE) enrichments (e.g. Marks et al. 2004; Reguir et al. 2012). The fractionation of such
80 HREE-rich Cpx from their parental magma may lead to the formation of HREE-rich
81 cumulates with economic concentrations (Möller and Williams-Jones 2016). Such HREE
82 enrichments of Cpx have been tentatively attributed to the preferential incorporation of HREE
83 in the VI-coordinated M1 site, whereas light and middle REE (LREE and MREE,
84 respectively) are preferentially incorporated in the VIII-coordinated M2 site (Bottazi et al.
85 1999; Fedele et al. 2009; Olin and Wolff 2010; Reguir et al. 2012, Beard et al. 2019). Cpx
86 enriched in HREE relative to MREE also display uncommon positive Zr and Hf anomalies
87 (e.g., Bakti et al. 2018; Baudouin et al. 2016; Marks et al. 2004; Weidendorfer et al. 2016).
88 These substitutional variations seem to occur for specific compositions (e.g., high Mn or Na
89 contents, usually in alkaline rocks), though HREE enrichments have been observed in both
90 aegirine ($\text{NaFe}^{3+}\text{Si}_2\text{O}_6$) and diopside ($\text{CaMgSi}_2\text{O}_6$) (Marks et al. 2004; Möller and Williams-
91 Jones 2016; Reguir et al. 2012; Weidendorfer et al. 2016; Beard et al. 2019). Subtle HREE

92 enrichments are also occasionally observed in basanite (Woodland and Jugo 2007) and in
93 silica-saturated rocks such as diorites (e.g., Zhang et al. 2017). Sinusoidal patterns of REE
94 partition coefficients are nevertheless not always observed for alkaline compositions. REE
95 partitioning between diopside and trachy-phonolite melt suggests that all REE are substituted
96 in the M2 site and no anomalous HREE distributions are observed (Mollo et al. 2016). Thus,
97 Cpx, enriched or not in HREE, can equilibrate with phonolitic compositions, implying that the
98 HREE-enrichments observed in some alkaline rocks may be dominated by the crystal-
99 chemical framework of Cpx rather by the melt composition.

100 In the present study, we address the partitioning of trace elements between Cpx and
101 silicate melt in alkaline systems, and the origin of HREE enrichments in Cpx from some
102 alkaline igneous complexes. We determined the trace element partition coefficients for Cpx
103 phenocrysts in equilibrium with phonolitic melt inclusions in ijolite cognate cumulates from
104 Oldoinyo Lengai that document the active magma chamber, in which HREE-rich Cpx have
105 previously been described (Mollex 2017). Based on our observed partition coefficient, we use
106 the lattice strain model to improve our understanding of the substitution parameters of trace
107 elements in the Cpx crystal sites (Blundy and Wood 1994). These new data are used alongside
108 D values from literature to elaborate general equations based on Cpx chemistry that provide
109 $D_i^{\text{Cpx/melt}}$ for REE and high field strength elements (HFSE; Ti, Hf, Zr, Nb, Ta) in alkaline
110 magmas.

111

112 **Sample and Methods**

113 **Sample description**

114

115 Oldoinyo Lengai is an active volcano that erupts both natrocarbonatite and alkaline
116 silicate magmas (Dawson 1998; Keller and Krafft 1990; Mollex et al. 2018). During the sub-
117 Plinian 2007–2008 eruption, various xenoliths including ijolite cognate cumulates were
118 brought to the surface, providing samples from the active magma reservoir (Mollex et al.
119 2018). This eruption was triggered by the recharge of the magmatic reservoir, and the ijolite
120 samples provide constraints from the mid-crustal reservoir (~13 km, 1000°C; de Moor et al.
121 2013; Baudouin and France 2019). We studied Cpx and Cpx-hosted melt inclusions in 3
122 ijolites (10TL01, 10TL05, 10TL06; Fig. A1), collected on the southern slope of the northern
123 active crater. We focus our study on sample 10TL01 which contains the largest melt

124 inclusions (Fig. 1). The volatile element content, liquid line of descent, crystallization
125 sequence, and origin of the sample were presented in detail by Mollex (2017).

126 Ijolite sample 10TL01 contains large crystals of Cpx, Ti-garnet (melanite), nepheline,
127 apatite and minor sulfides, titanomagnetite, wollastonite, and interstitial glass. A single
128 population of Cpx phenocrysts (100-1000 μm) is present in the studied sample, it displays a
129 slightly patchy zoning with a restricted compositional variation (Fig. A1). Melt inclusions in
130 Cpx are relatively small ($\leq 50 \mu\text{m}$), and their hosting Cpx show local chemistry variation (Fig.
131 1d). To minimize the effect of the local chemistry variation, Cpx-melt couples were analyzed
132 very close to each other; melt-Cpx composition covariations will help us quantifying the
133 dependence on composition of partition coefficients. $\sim 10\%$ of the Cpx-hosted melt inclusions
134 also contain small amount of carbonatite globule ($< 2\%$ vol. of the whole melt inclusion
135 volume), those inclusions have not been considered to estimate silicate melt - Cpx
136 partitioning. Detailed petrographic observations have also shown that some melt inclusions
137 contains daughter mineral (e.g., magnetite), and have therefore also not been considered to
138 quantify melt - Cpx partitioning. Among the selected melt inclusions ($n=16$), Cpx have
139 homogeneous composition around the melt inclusions, except for 1 Cpx-melt couple which
140 displays a lighter shade in the BSE image (Fig. 1c, cpx n°1 on table S1).

141

142 **Major and trace element measurements**

143

144 Major element concentrations in Cpx and glasses were determined using a CAMECA
145 SX-100 electron microprobe at the Laboratoire Magmas et Volcans (LMV, Clermont-Ferrand,
146 France). Analyses were performed using a 15 kV accelerating voltage. Minerals were
147 analyzed using a focused beam and a 6 nA current, whereas melt inclusion measurements
148 were performed using a spot size of 5 μm and a 4 nA current to prevent host mineral
149 contamination and minimize alkali loss and beam damage of the glasses (errors in
150 supplementary material).

151 Trace element concentrations were determined using a Thermo Element XR laser
152 ablation inductively coupled plasma mass spectrometer at LMV. Laser beam diameters of 25
153 and 9 to 15 μm were used for Cpx and melt inclusions, respectively, with a laser repetition
154 rate of 1–2 Hz and laser power of $4.8 \text{ J}\cdot\text{cm}^{-2}$ (laser excimer 193 nm Resonetics M-50E). Trace
155 element concentrations were calibrated by using similar laser beam diameters, and
156 international standard glasses NIST612 as primary standard, and NIST610 and BCR-2 as
157 secondary standards; the SiO_2 and CaO concentrations previously determined by electron

158 microprobe for individual Cpx and glasses were used as internal standards (errors and
159 standards in supplementary material). The Glitter Software (Griffin et al. 2008) was used to
160 process the raw data files of signal intensity versus time.

161

162 **Results**

163 **Clinopyroxene chemistry**

164

165 Cpx from Oldoinyo Lengai ijolites occur as large crystals (100–1000 μm) with
166 diopside to augite compositions ($\text{Wo}_{48}\text{En}_{38}\text{Fs}_{14}$ to $\text{Wo}_{44}\text{En}_{27}\text{Fs}_{29}$), and relatively low aegirine
167 components (Ae_6 to Ae_{21}) (Fig. 2). Cpx Mg# ($= 100 \times \text{Mg}/(\text{Mg}+\text{Fe})$ in molar proportions)
168 range from 49 to 74 with relatively high Fe content (8.2–16.0 wt% FeO_t). Minor element
169 contents are 0.4–0.7 wt% Al_2O_3 , 0.3–0.46 wt% TiO_2 , 0.25–0.49 wt% MnO , and 1.0–2.5 wt%
170 Na_2O (Fig. 3a, Table S1). Fe^{3+} contents calculated using the stoichiometric method (Droop,
171 1987) are slightly lower than Fe^{2+} contents ($\text{Fe}^{3+} = 0.05\text{--}0.22$ per formula unit, p.f.u., vs. Fe^{2+}
172 $= 0.14\text{--}0.36$ p.f.u.; Fig. 3b). The T site is occupied by silicon with minor Al^{IV} (0.01–0.03) and
173 Fe^{3+} (0–0.03), the M1 site incorporates Fe^{3+} , Fe^{2+} , Mg^{2+} , Ti^{4+} , and Mn^{2+} cations, and the M2
174 site is filled by $\text{Ca}^{2+} + \text{Na}^+$ ($= 1$ p.f.u.).

175 Cpx REE contents, when normalized to chondrite, are characterized by a sinusoidal
176 pattern with a strong HREE enrichment. Cpx have low REE contents (e.g., 0.67–1.65 ppm La;
177 corresponding to 2–8 times chondritic values) and are enriched in LREE and HREE compared
178 to MREE ($(\text{La}/\text{Dy})_{\text{N}} = 2.6\text{--}5.4$ and $(\text{Lu}/\text{Ho})_{\text{N}} = 6.2\text{--}8.8$, where the subscript ‘N’ denotes
179 chondrite-normalized values, McDonough and Sun (1995) (Figs. 4a, A2). Cpx have high
180 incompatible element concentrations, with Sr varying from 547 to 720 ppm, Zr from 174 to
181 354 ppm, and low concentrations of Sc (2.7–4.3 ppm) and Nb (0.1–0.3 ppm) (Table S2). Cpx
182 have a distinct positive Zr-Hf anomaly relative to the primitive mantle, as evidenced by
183 $(\text{Hf}/\text{Sm})_{\text{N}}$ ratios of 16.4–27.7 (Figs. 4b, A2 & A3).

184

185 **Phonolite melt inclusions**

186

187 Cpx-hosted melt inclusions have phonolitic compositions with SiO_2 contents varying
188 from 47.3 to 50.4 wt%, alkali ($\text{Na}_2\text{O} + \text{K}_2\text{O}$) from 17.8 to 21.9 wt% (Fig. 5, Table S1), and
189 very low MgO contents ranging from 0.03 to 0.38 wt%. CaO content varies from 0.54 to 2.09
190 wt%, FeO_t from 5.2 to 9.6 wt%, and Al_2O_3 from 10.9 to 17.7 wt% (Table S1). Melt inclusions
191 have high REE contents, with La varying from 40 to 210 ppm (200–1000 times chondritic

192 values, McDonough and Sun 1995), and are enriched in LREE compared to HREE with
193 La/Yb varying from 8 to 38. Melt inclusions have high incompatible element concentrations
194 with Sr contents ranging from 650 to 3730 ppm, Nb from 420 to 850 ppm, and Zr from 700 to
195 3180 ppm (Table S2, Fig. A2; A3).

196

197 **Trace element partitioning**

198

199 Cpx/phonolite melt trace element partition coefficients have been calculated from the
200 concentrations measured in 16 Cpx-hosted melt inclusions and their Cpx hosts. However,
201 melt inclusion compositions may be affected by post-entrapment crystallization, modifying
202 the Cpx-melt equilibrium. If extensive, post-entrapment crystallization could result in the
203 under- or over-estimation of partition coefficients for incompatible and compatible elements,
204 respectively. The contribution of post-entrapment crystallization in the studied melt inclusions
205 has been estimated to be ~9% based on experimentally determined Fe-Mg partition
206 coefficients and DiHd composition parameter (Masotta et al. 2013; Mollo et al. 2013; details
207 in supplementary material). For incompatible elements, post-entrapment crystallization of a
208 few percent Cpx at melt inclusion margins does not modify the melt composition by more
209 than few percent for incompatible elements (see calculation in supplementary material; Fig.
210 A4). Taking in account both Analytical errors and post-entrapment crystallization, we
211 estimate that our reported partition coefficients are accurate to within 10% (analytical errors
212 in supplementary material).

213

214 Compared to literature data associated with basalts or phonolites (Adam and Green
215 2006; Hill et al. 2000; Mollo et al. 2016), the REE partition coefficients between Cpx and
216 phonolite melt obtained herein 1) are significantly lower, 2) increase from LREE to MREE
217 ($D_{La} = 0.013 \pm 0.005$ and $D_{Sm} = 0.062 \pm 0.018$, respectively), and from MREE to HREE (D_{Ho}
218 $= 0.062 \pm 0.021$ and $D_{Lu} = 0.41 \pm 0.14$, respectively) (Fig. 6; Tables 1, S3), and 3) D_{HREE} such
219 as D_{Lu} is not correlated with D_{LREE} (e.g., D_{La}), but displays a slight correlation with other
220 trivalent cation partition coefficients like with D_{Sc} (Tables 1, S3).

221 The low LREE and MREE partition coefficients observed for alkaline magmas herein
222 and in previous studies (Adam and Green 2006; Dalou et al. 2012; Hill et al. 2000; Mollo et
223 al. 2016; Fig. 6) imply a strong REE enrichment of the residual liquid during Cpx
224 crystallization. These uncommon partition coefficients associated with alkaline systems

225 therefore result in very high REE contents in the associated evolved melts (e.g., trachy-
226 phonolite, phonolite, carbonatite).

227 Tetraivalent HFSE have D values close to D_{HREE} (e.g., $D_{\text{Zr}} = 0.13 \pm 0.06$ and $D_{\text{Hf}} = 0.25$
228 ± 0.1), similar to those observed for trachy-phonolite melt (Mollo et al., 2016) (Fig. 6, Table
229 1). Pentavalent HFSE have very low D values (e.g., $D_{\text{Nb}} < 0.0005$ and $D_{\text{Ta}} < 0.003$). Zr and Hf
230 have higher partition coefficients than MREE, as highlighted by high $D_{\text{Hf}}/D_{\text{Nd}}$ ratios (2–5.6;
231 Fig. 7). Other Cpx trace element partition coefficients are as follows: $D_{\text{Sr}} = 0.66 \pm 0.23$, $D_{\text{Ba}} =$
232 0.0002 ± 0.00006 , $D_{\text{Th}} = 0.0003 \pm 0.0001$, and $D_{\text{V}} = 0.63 \pm 0.33$ (Table 1). In this study, we
233 observe that Sr is only moderately incompatible and has a high partition coefficient relative to
234 REE (Fig. A2), whereas Sr behaves more incompatibly in basaltic melts (Fig. 6).

235

236 Discussion

237 Lattice strain model parameters

238

239 Partition coefficients D_i can be modeled using lattice strain theory (Blundy and Wood,
240 1994) as:

$$241 \quad D_i = D_0 \exp \left[\frac{-4\pi EN_A \left[\frac{r_0}{2}(r_i - r_0)^2 + \frac{1}{3}(r_i - r_0)^3 \right]}{RT} \right] \quad (1)$$

242

243 where D_i is a function of the cation radius (r_i), the partition coefficient (D_0) of the ideal cation
244 with a radius r_0 (Å) for the crystallographic lattice M1 or M2, and an elastic constant E
245 (Young's modulus, in GPa), as well as Avogadro's constant N_A ($6.022 \times 10^{23} \text{ mol}^{-1}$), the
246 universal gas constant R ($8.3145 \text{ J} \cdot \text{mol}^{-1} \cdot \text{K}^{-1}$), and temperature T (Kelvin). In Cpx, the six-
247 fold coordinated M1 site incorporates tetravalent (Ti^{4+} , Zr^{4+} , Hf^{4+}) and trivalent cations (e.g.,
248 Cr^{3+} , Sc^{3+}) whereas the eight-fold coordinated M2 site preferentially incorporates REE^{3+} (e.g.,
249 Adam and Green 2006; Blundy and Wood 1994, 2003; Dalou et al. 2012; Hill et al. 2000).
250 Detailed calculation of the strain energy in the lattice strain model (LSM) is provided in the
251 supplementary material.

252 Trace element partitioning between Cpx and melt ($D_i^{\text{Cpx/melt}}$) has been characterized
253 and quantified by applying the LSM (Onuma et al. 1968) to various Cpx and melt
254 compositions (e.g., Blundy et al. 1998; Gaetani and Grove 1995; Wood and Blundy 1997,
255 2001). In order to determine the effects of melt composition, Cpx chemistry, pressure, and
256 temperature on partition coefficients, we compared our D values measured from Oldoinyo
257 Lengai ijolite to a dataset including Cpx in equilibrium with phonolite (Mollo et al. 2016;

258 Olin and Wolff 2010), basalt (e.g., Dalou et al. 2012; Hill et al. 2000), and basanite melts
259 (Adam and Green 2006). The LSM was applied to those D values using the SIMPLE FIT and
260 DOUBLE FIT program (Dalou et al. 2018), which calculates the best-fit values of the lattice
261 strain parameters (r_0 , D_0 , and E) for both clinopyroxene M-sites. DOUBLE FIT does not
262 require assignments of elements per site or constraints on the LSM parameters to calculate the
263 best-fit values and LSM parameters. However, we considered HREE³⁺ as being either 6- or 8-
264 fold coordinated (i.e., in the M1 or M2 site in Cpx, respectively) when fitting the REE data
265 (see section 5.1.1). To obtain reliable estimates of r_0 , D_0 , and E , DOUBLE FIT requires a
266 minimum of six D_i values: we therefore focused our study on the partitioning of trivalent
267 (REE³⁺, Cr³⁺, Sc³⁺). For tetravalent cations (Ti⁴⁺, Zr⁴⁺, Hf⁴⁺), we use SIMPLE FIT (minimum
268 of 3 D_i values) to determine M1 LSM parameters.

269

270 *REE and trivalent cations*

271

272 Previous studies have successfully applied the LSM to Cpx-melt partitioning, and the
273 distribution of REE can be modeled by assuming that all REE are substituted for Ca in the M2
274 site (e.g., Hill et al. 2000; Mollo et al. 2016; Wood and Blundy 1997). Between Mg-rich Cpx
275 and basaltic liquid, LREE are highly incompatible ($D_{La} \leq 0.1$), and incompatibility
276 decreases toward the MREE with relatively constant D values between Ho and Lu (e.g.,
277 Wood and Blundy 2007; Hill et al. 2000; Wood and Blundy 1998) (Fig. 8). In contrast, the
278 $D_{REE}^{Cpx/phonolite}$ values obtained herein are not consistent with the existing models (e.g. Blundy
279 and Wood 1994); assuming incorporation of all REE in the M2 site: indeed HREE (Er to Lu)
280 do not follow a parabolic repartition commonly explained by the LSM (Fig. 8), implying the
281 substitution of HREE in both the M2 and M1 sites. It is therefore necessary to estimate D_0 , r_0 ,
282 and E for trivalent cations in both the M1 (HREE³⁺, Sc³⁺, Cr³⁺) and M2 sites (HREE³⁺,
283 MREE³⁺, LREE³⁺, Fig. 8), which provides lattice strain parameters that differ significantly
284 from the literature data (Bédard 2014; Dygert et al. 2014, Fedele et al. 2009; Olin and Wolff
285 2010). HREE incorporation in M1 have been previously suggested, but predictive model
286 for D_{HREE} must be carefully determined yet.

287 Cpx-phonolite melt D_0^{3+} parameters for the M2 site are very low ($D_0^{3+} = 0.07 \pm 0.015$)
288 relative to those obtained by Mollo et al. (2016); ($D_0^{3+} = 1.07 \pm 0.27$; Table S4). Previous
289 studies have shown the strong influence of Cpx Al^{IV} content on the D_0^{3+} value of the M2 site
290 (e.g., Hill et al. 2000; Mollo et al. 2016; Wood and Blundy 1997). The very low D_0^{3+} value

291 obtained herein can thus be related to the very low Al^{IV} content of Oldoinyo Lengai Cpx
292 (≤ 0.03 p.f.u., Table S1). The LSM parameters obtained herein are also characterized by
293 relatively high r_0^{M2} (i.e., 1.05 Å), and E^{M2} values within the range of previous studies related
294 to low pressure ($E = 325\text{--}441$ GPa; Hill et al., 2000; Mollo et al. 2016; Tables 2, S4, S5).

295 The LSM parameters for the M1 site are $D_0^{3+} = 1.24 \pm 0.44$, $E^{3+} = 382 \pm 48$ GPa, and
296 $r_0^{3+} = 0.74 \pm 0.006$ Å (Table 2, Fig. 9). D_0^{3+} and E are inter-correlated and display very low
297 values compared to other studies of basaltic to phonolitic compositions (Dalou et al. 2012;
298 Hill et al. 2000; Olin and Wolff 2010). The ideal cation radii (r_0) are among the largest
299 reported, except those for HREE-bearing M1 sites from Olin and Wolff (2010) ($r_0^{M1} = 0.72\text{--}$
300 0.77 Å). HREE incorporation in the M1 site thus seems to be promoted by high r_0^{3+} (>0.7 Å)
301 and low E^{3+} (<500 GPa) of this crystallographic site (Figs. A5, A6, A7).

302

303

HFSE

304

305 HFSE (4+ and 5+ cations) are commonly considered to be incorporated in the M1 site
306 (i.e., six-fold coordination; e.g., Wood and Blundy 2007). By studying their partitioning
307 behavior, we obtain information on the properties of the M1 site, and on their dependence on
308 Cpx chemistry (Figs. 10 A6). Due to the very low partition coefficients for Nb and Ta (e.g.,
309 $D_{Nb} = 0.0001\text{--}0.0005$) and uncertainties on the valence of vanadium (3+, 5+; Adam and
310 Green, 2006), we applied the LSM only for tetravalent (Ti^{4+} , Zr^{4+} , Hf^{4+}) and not pentavalent
311 HFSE. Obtained LSM parameters are $D_0^{4+} = 0.73\text{--}1.08$, $E^{4+} = 1736\text{--}2397$ GPa, and $r_0^{4+} =$
312 $0.655\text{--}0.662$ Å (Table 2, Fig. A8). The r_0^{4+} of the M1 site correlates with Cpx chemistry (Fig.
313 A8) but is particularly large when compared to values of previous studies (e.g., Blundy et al.
314 1997; Hill et al. 2000; Mollo et al. 2016; 2018), particularly. The D_0 and E values obtained
315 herein are lower than those for Mg-Al rich Cpx (Hill et al. 2000; Table S5) and similar to
316 those of Fe-rich Cpx (Dygert et al. 2014).

317

Factors controlling trace element partitioning in Cpx

318

319
320 The specific features of Cpx trace element compositions, and of the associated
321 partition coefficient distribution determined herein (e.g., HREE and Zr-Hf enrichments
322 relative to MREE in Cpx, as well as their covariation highlighted by a well-defined $(Zr/Nd)_n$
323 vs $(Lu/Ho)_N$ correlation; Fig. 7a) are observed in several other alkaline complexes (Figs. 4,
324 7a). In this study, these anomalies are associated with higher D_{Zr}/D_{Nd} and D_{Lu}/D_{Ho} ratios

325 compared to the literature (D_{Zr}/D_{Nd} and $D_{Lu}/D_{Ho} < 1.2$, Fig. 7b; Adam and Green 2006; Hill et
326 al. 2011; Mollo et al. 2016).

327 The partitioning of trace elements between Cpx and melt varies with intensive
328 parameters (pressure, temperature, redox conditions), melt composition, and Cpx chemistry
329 (e.g., Bennett et al. 2004; Blundy et al. 1998; Hill et al. 2011; Olin and Wolff 2010).

330 Pressure and temperature are expected to have a strong effect on ideal cation radius
331 (r_0) and partition coefficients (e.g., Hill et al. 2011). However, Cpx-melt partition coefficients
332 acquired over a large pressure and temperature range do not display an effect on HREE
333 partitioning in the M1 site for basalts (Adam and Green 2006; Dalou et al. 2012; Hill et al.
334 2000) or even trachy-phonolite melt equilibrated in the same pressure range as our study
335 (≤ 350 MPa; Mollo et al. 2016). The low equilibrium D_0^{M2} values determined herein at low
336 pressure and moderate temperature conditions (~ 300 MPa and 1050 °C) should therefore be
337 attributed to other parameters.

338 Melt composition (e.g., silica, alkali, or volatile contents) influences the melt structure,
339 and trace element partition coefficients usually decrease with increasing melt polymerization
340 (characterized by the number of non-bridging oxygens per tetrahedral cation, NBO/T; Gaetani
341 2004; Huang et al. 2006, Michely et al. 2017, Mollo et al., 2016; Figs. A9 & A10). According
342 to those studies, an increasing in NBO/T value would imply an important decrease of the
343 partition coefficients down to one order of magnitude (when NBO/T rises from 0.2 to 2).
344 However, There is no correlation between NBO/T and HREE enrichment for phonolite and
345 basalt melts (e.g., NBO/T = 0.61–0.8 at $D_{Lu}/D_{Er} > 5$ for phonolite and NBO/T = 0.5–0.7 at
346 $D_{Lu}/D_{Er} = 0.93$ –1.17 for basalts; Gaetani, 2004). In the case of $D_{HREE} > D_{MREE}$ (Beard et al.
347 2019; Olin and Wolff 2010, this study), the melt polymerization and composition effect on
348 partition coefficient seems to be negligible in comparison to the effect of mineral chemistry
349 (Figs. A10). Michely et al. (2017) observe correlations between melt Na_2O content and trace
350 element partition coefficients. The influence of Na over trace element partitioning may apply
351 only in the case of Na-poor melts (0–2.5 wt% Na_2O), since we do not observe any relationship
352 between Na_2O or K_2O content in our melts (varying between 6 and 13 wt%) and trace element
353 partition coefficients (Fig. A10).

354 HREE enrichment in Cpx is therefore not related to specific pressure conditions or
355 melt composition (basalt/phonolite), but can likely be related to the Cpx chemistry. Partition
356 coefficient values have been shown to rise with increasing Al^{IV} content (Gaetani and Grove
357 1995, and Lundstrom et al. 1994, Wood and Blundy 1997). In addition, HREE enrichment
358 in Mn-rich Cpx ($MnO = 2.4$ –2.9 wt%) negatively correlates with Fe^{2+} and positively

359 correlates with Mn^{2+} content (Olin and Wolff 2010). Cpx Na content may also exert a
360 dominant control on REE partitioning following the substitution $Na^+ + REE^{3+} = 2 Ca^{2+}$ (Wood
361 and Blundy 1997), although this correlation has only been observed for extremely Na-rich
362 Cpx (2.2–13.5 wt% Na_2O) at high-pressure conditions (>3 GPa; e.g., Bennett et al. 2004). The
363 role of Cpx chemistry, observed at high pressure, needs to be further investigated for Na-rich
364 clinopyroxenes crystallized at low pressure (see the discussion below).

365 Here we have used a $D^{Cpx/melt}$ dataset for melt compositions ranging from basalt to
366 phonolite, with and without HREE anomalies, to track the origin of the anomalous partition
367 coefficients observed in various alkaline complexes (Figs. 4–7; Adam and Green 2006; Dalou
368 et al. 2012; Hill et al. 2000; Mollo et al. 2016; Olin and Wolff 2010). LSM parameters are
369 correlated with high D_{HREE}/D_{MREE} : specifically, high r_0^{3+} values for the M1 site (0.73–0.75 Å)
370 are well correlated to Cpx chemistry (e.g. Mg/Fe and Na/Ca ratios) and to the HREE
371 enrichment (Fig. 9, A6, A7), that can be quantified by the parameter Lu^* (see section 5.3.1 for
372 further details):

$$373 \quad Lu^* (\%) = [D_{Lu}^{M1} / (D_{Lu}^{M1} + D_{Lu}^{M2})] \times 100 \quad (2)$$

374 In the M1 site, r_0^{3+} increases along with Fe^{3+} content and decreases with Mg^{2+} and
375 Al^{IV} contents increase (Fig. 9, Table S5), whereas E^{3+} is negatively correlated with r_0^{3+} and
376 increases along with Mg content (Fig. A7). Cameron and Papike (1980) showed that the
377 nature and size of the main cation in the M2 site has an influence on the ionic radius of the
378 M1 site. In the present study, the ionic radius of the M1 site is sensitive to Mg/Fe and
379 Fe^{3+}/Fe^{2+} ratios. In the absence of Al (i.e., the jadeite pole), Na^+ atoms are charge balanced
380 with Fe^{3+} (i.e., the aegirine pole) as observed herein and at various alkaline complexes (Fig.
381 2). As r_0^{3+} in the M1 site is strongly dependent on Mg and Fe^{3+} content and well correlated
382 with HREE enrichment (high Lu^* ; Fig. 9), aegirine and Mg contents seem to be the main
383 chemistry factors inducing HREE incorporation in the M1 site. HREE enrichments should
384 therefore be prevalent in the presence of Fe^{3+} in Cpx (thus under oxidizing conditions), and in
385 alkaline magmatic systems that allow charge balance between trivalent (Fe^{3+}) and monovalent
386 (Na^+) cations instead of two bivalent cations ($Mg^{2+} + Ca^{2+}$; the diopside pole). Furthermore,
387 Cpx crystals may record magmatic differentiation with Fe-rich and more oxidized (Fe^{3+} -rich)
388 composition, leading to significant enrichment in HREE and high Hf/Sm ratios (Woodland
389 and Jugo 2007).

390 The observed high $D_{\text{HREE}}/D_{\text{MREE}}$ are strongly correlated with high D_{Zr} and D_{Hf} values
391 relative to MREE (e.g., $D_{\text{Hf}}/D_{\text{Sm}}$ and $D_{\text{Zr}}/D_{\text{Nd}} > 2$; Figs. 6, 7). This is mostly due to the low
392 D_{MREE} values, as the partition coefficients of Zr and Hf are within the range of literature data
393 (Fig. 6). $D_{\text{Zr}}/D_{\text{Nd}}$ increases with increased r_0^{4+} in the M1 site, which is related to increased
394 Fe^{3+} content and decreased Al^{IV} and Mg contents (Fig. A8).

395

396 **Parameterization of the trace element distribution**

397 *Prediction of HREE enrichment*

398

399 In the following section, we propose a parameterization based on Cpx major element
400 composition only that allows prediction of Cpx HREE enrichment (high $D_{\text{Lu}}/D_{\text{Ho}}$; Fig. 11),
401 and associated partition coefficients. Neither trace element quantification, nor melt
402 composition are required to proceed with D estimate. Parameterization constants along with
403 the corresponding spreadsheet built to predict REE partitioning between clinopyroxene and
404 alkaline evolved melts are provided in supplementary material, and described below. Data
405 used for the parameterization are from this study, Adam and Green (2006); Dalou et al.
406 (2012); Hill et al. (2000); Mollo et al. (2016) and Olin and Wolff (2010).

407 Parameters that may influence HREE enrichment (i.e., Lu^*) such as pressure,
408 temperature, and composition were tested using a multiple linear regression (Excel Analysis
409 “ToolPak”) to determine the main influencing variables. As Lu^* is well correlated with r_0^{M1}
410 and Cpx chemistry (Figs. 9, A6), we further quantify the observed HREE enrichment as a
411 function of the main influencing cation contents (Mg, Ca, Fe, Al). The impact of each major
412 element and estimated temperature on Lu^* is best reproduced by the following equation:

413

$$414 \quad \text{Lu}^* = a_{\text{Lu}} T + b_{\text{Lu}} \text{Fe}^{3+} + c_{\text{Lu}} \text{Al}^{\text{VI}} + d_{\text{Lu}} \text{Mg} + e_{\text{Lu}} \text{Ca} + g_{\text{Lu}} \quad (r^2 = 0.84), \quad (3)$$

415

416 where element contents are expressed in formula units (calculated with 6 oxygen atoms),
417 temperature in °C, and the fit parameters are $a_{\text{Lu}} = 0.098$, $b_{\text{Lu}} = 175$, $c_{\text{Lu}} = -222.07$, $d_{\text{Lu}} = -$
418 97.81 , $e_{\text{Lu}} = 57.59$, $g_{\text{Lu}} = -41.73$ (Table S6). This parameterization is calibrated over a range
419 of Cpx compositions (expressed in moles p.f.u., $\text{Fe}^{3+} = 0-0.3$, $\text{Al}^{\text{VI}} = 0-0.3$, $\text{Mg} = 0.2-0.9$, $\text{Ca} =$
420 $0.5-1$), and temperatures (700-1400°C). Equations similar to equation (3) are obtained for the
421 other HREE (Er^* , Tm^* , and Yb^*) with the parameters provided in Table S6.

422 The equation (3) and fit parameters presented in Table S6 highlight the significant role
423 of Fe^{3+} and Mg, and to a lesser extent those of temperature, Al^{VI} , and Ca, in influencing
424 HREE partitioning in Cpx. As the Lu^* , Er^* , Tm^* , and Yb^* parameters are based mainly on
425 the Cpx major element composition, they can be calculated to predict anomalous HREE
426 enrichment for any Cpx crystal. The reliability of our parameterization was tested using
427 $(\text{Lu}/\text{Ho})_{\text{N}}$ ratios in Cpx from various alkaline provinces worldwide; alkaline syenites, Bakti et
428 al. 2018; Marks et al. 2004; Möller and Williams-Jones 2016; Vuorinen et al. 2005;
429 nephelinites, Baudouin et al. 2016; Weidendorfer et al. 2016; and phonolites, Baudouin and
430 Parat 2015). This independent set of data show a very good correlation between the Lu^*
431 parameter calculated with equation (3) based on major elements only, and the observed HREE
432 enrichment expressed by the ratio $(\text{Lu}/\text{Ho})_{\text{N}}$ of natural Cpx (Fig. 12 ($r^2=0.8$)).

433

434 *Prediction of REE element partitioning*

435

436 By quantifying the Lu^* , Er^* , Tm^* , and Yb^* parameters, we can then determine
437 anomalous D values for those elements from Cpx major element compositions, P , T and
438 $\text{Mg}^{\# \text{melt}}$. HREE* and LSM parameters on M2 can be used to quantify D_{REE} without using
439 LSM parameters of the M1 site, when data available from literature to apply a well constrain
440 multiple regression are too rare.

441 Mollo et al. (2016) adapted the LSM equations proposed by Wood and Blundy (1997)
442 for REE partitioning between Cpx and trachy-phonolite magmas. Their model quantifies
443 REE^{3+} partitioning between melt and the M2 site of Cpx: D_0^* is obtained from pressure, T ,
444 $\text{Mg}^{\# \text{melt}}$, and $X_{\text{Mg}}^{\text{Cpx}}$, when r_0^* and E^* are calculated from $X_{\text{Ca}}^{\text{Cpx}}$ and $X_{\text{Mg}}^{\text{Cpx}}$ (where $X_{\text{Mg,Ca}}^{\text{Cpx}}$
445 represents the mole fraction of each element in Cpx; Fig. A11). We applied equations from
446 Wood and Blundy (1997), Mollo et al. (2016) and Beard et al. 2019 to our Cpx-melt pairs
447 (Fig. 13). Wood and Blundy (1997) and Mollo et al. (2016) successfully reproduce the
448 measured LREE and MREE partition coefficients (from La to Ho), but significantly
449 underestimate those of HREE (Er, Tm, Yb, Lu). Beard et al. (2019) model strongly
450 overestimate all REE partition coefficients and only reproduce correctly D_{Lu} (Figs. 13, A11).
451 Beard et al. (2019) model manages to predict D_{REE} within 1 order of magnitude of confidence
452 for most of basaltic to phonolitic melt compositions (with pressure, temperature and Cpx
453 major element composition as input parameters; Fig. A12). Nevertheless we believe that one
454 order of magnitude of confidence is too large when considering partition coefficients and

455 related igneous petrology models. Beard et al. (2019) models display important discrepancy
 456 between measured and predicted partition coefficients at a smaller scale (Fig. A12). In order
 457 to improve those previous calibrations we present hereafter a new model to account for the
 458 identified discrepancies.

459

460 The partition coefficient of Lu can be modeled as a function of the Lu* parameter, D_0^*
 461 and E^* (M2 site) as:

462

$$463 \quad D_{Lu} = h_{Lu} Lu^* + j_{Lu} D_0^* + k_{Lu} E^* + l_{Lu}. \quad (4)$$

464

465 where $h_{Lu} = 0.008$, $j_{Lu} = 0.76$, $k_{Lu} = -0.0018$, and $l_{Lu} = 0.62$. Equations similar to equation (4)
 466 can be obtained for Er*, Tm*, and Yb* by using the fit parameters presented in the Table S6.
 467 D_0^* and E^* are obtained using equations (5)-(6)-(7) presented below.

468

469 The partition coefficients estimated using equation (4) are relevant when Lu* (or Er*,
 470 Tm*, Yb*) > 40% (HREE incorporated in both sites). Fig. 13 highlights the improvement of
 471 this approach in determining D_{HREE} when Lu* > 40%. When HREE enrichment is low (i.e.
 472 Lu* < 40%), we recommend to calculate D_{HREE} from Mollo et al. (2016) approach, that was
 473 calibrated for phonolitic and trachy-phonolitic melts (spreadsheet for details).

474

475 In equation (4), D_0^* and E^* for trivalent cations (M2 site) are obtained by using equation (5)
 476 and (6) (Wood and Blundy 1997; Mollo et al. 2016):

$$477 \quad D_0^* = \frac{Mg\#_{melt}}{XMg^{M1}} * \exp\left(\frac{88750 - 65.644 * T + 7050P - 770P^2}{RT}\right) \quad (5)$$

$$478 \quad E^* = -82.35 + 636.56 * X_{Ca}^{cpX} - 253.29 * X_{Mg}^{cpX} \quad (\text{GPa}) \quad (6)$$

479

480 However, those equations require knowledge of the melt composition to obtain D_0^* and thus
 481 D_{REE} . In order to facilitate the use of our new model, we propose that for phonolite and
 482 trachyte compositions and for a range of temperature from 840 to 1020°C, D_0^* can be
 483 expressed as a function of Al_{Cpx}^{IV} only (for $Al_{Cpx}^{IV} < 0.15$ p.f.u.), facilitating the use of the
 484 proposed parametrization (Fig. A13) as:

485

$$486 \quad D_0^* = 10.434 \times Al_{Cpx}^{IV} + 0.0384. \quad (r^2 = 0.93) \quad (7)$$

487

488 D_0^* calculated from Al_{Cpx}^{IV} is relevant for a smaller range of Cpx composition than equation
489 (5), however Cpx with low Al^{IV} content ($Al_{Cpx}^{IV} < 0.15$ p.f.u) is common in alkaline rocks
490 (syenite, phonolite, alkali-rich nephelinite, Fig 3b). Furthermore, Cpx with low Al content and
491 moderate aegirine content are often related to alkaline igneous complexes associated with
492 carbonatites (Marks et al. 2004, Weidendorfer et al. 2016, Vuorinen et al. 2005). Finally the
493 parametrization of REE partition coefficients between alkaline melt and Cpx that is proposed
494 herein allows one to obtain D_{REE} from major element composition of Cpx only, T should also
495 be estimate (spreadsheet available in supplementary table).

496

497

498 *Determination of HFSE partition coefficients*

499

500 The parameterization of HFSE partition coefficients can also be improved for the
501 phonolite and trachy-phonolite alkaline magmas studied herein and in Mollo et al. (2016). We
502 revisited the covariations between D_{Ta} and Al^{IV} , D_{Hf} and D_{Zr} , D_{Ti} and D_{Zr} , and D_{Ti} and Al^{IV}
503 previously identified by Wood and Blundy (2007) in Fig. 10 by using the new partitioning
504 data presented herein and data from Mollo et al. (2016)(spreadsheet available in
505 supplementary table). The corresponding new equations valid for alkaline magmas are:

506

$$507 \quad D_{Ta} = 2.1976 \times (Al^{IV})^{1.9828}, \quad (r^2 = 0.83) \quad (8)$$

$$508 \quad D_{Ti} = 12.231 \times Al^{IV} + 0.1228. \quad (r^2 = 0.79) \quad (9)$$

$$509 \quad D_{Zr} = (D_{Ti} + 0.1268) / 5.905 \quad (r^2 = 0.69) \quad (10)$$

$$510 \quad D_{Hf} = 1.0823 \times D_{Zr} + 0.2015, \quad (r^2 = 0.95) \quad (11)$$

511

512 **Implications for REE evolution in alkaline magmatic systems**

513

514 Trace element contents of melts strongly increase during protracted fractional
515 crystallisation from mafic to highly alkaline magmas (i.e. phonolite), leading to the formation
516 of the critical metal deposits (e.g., Nb, REE) that are associated with carbonatites and silicate
517 alkali-rich magmas (e.g., Mountain Pass, USA; Ilmaussaq, Greenland). The budget of REE
518 and HFSE in evolved melts strongly depends on the crystallized phase assemblage, and on
519 their related partition coefficients. Cpx is a common mineral in alkaline magmas, and thus has

520 a major impact on their liquid line of descent, and on the one of associated carbonatites. The
521 new partition coefficients presented herein highlight that HREE-rich Cpx likely form with the
522 potential to promote LREE/HREE fractionation during magmatic differentiation. LREE-rich
523 residual evolved melts, and associated high HREE/MREE Cpx cumulates can thus be
524 produced (Fig. 14). Differentiation of phonolite melts may thus lead to evolved melts with
525 similar HREE contents than that of mined carbonatites and thus clearly represent potential
526 economic interests (Fig. 14). Cpx is not the only phase to crystallise from alkaline evolved
527 magmas, and additional minerals such as nepheline, mica, sodalite, feldspar must be
528 considered to quantify properly REE evolution in alkaline systems (e.g., Braunger et al. 2018,
529 Marks et al. 2004, Vuorinen et al. 2005.). Crystallization of accessory minerals such as
530 wollastonite, apatite, titanite may also have a huge impact on REE distribution between melts
531 and cumulates Fig. 14).

532

533 **Conclusions**

534

535 Our study highlights the low LREE and MREE partition coefficients and relative
536 HREE enrichment of Cpx crystallized from alkaline melts (phonolite). We have characterized
537 REE partitioning between Cpx and melt by applying the lattice strain model. HREE
538 enrichments are well correlated with the ideal ionic radius for trivalent cations r_0^{3+} in the M1
539 site, which is strongly dependent on Cpx chemistry: r_0^{3+} increases with increasing Fe^{3+}
540 content and decreases with increasing Mg^{2+} and Al^{VI} contents. This dependence of HREE
541 partitioning on Cpx chemistry allowed us to quantify HREE enrichment as a function of the
542 main influencing major element cation contents (Mg, Ca, Fe, Al) and temperature.

543 In our study, we proposed equations to predict HREE partitioning between Cpx and alkaline
544 melts without trace element measurements or knowledge of the exact melt composition.
545 Finally, we improved the parameterization of HFSE partition coefficients for phonolite and
546 trachy-phonolite alkaline magmas. A spreadsheet designed to apply the various models
547 presented herein is provided as supplementary material.

548 Those results suggest that when considering alkaline series, the likely large
549 LREE/HREE fractionation that may develop during Cpx or wollastonite crystallization could
550 eventually produce cumulates enriched in HREE, and residual melts enriched in LREE that
551 can then evolve to alkali-rich silicate melts and/or carbonatitic magmas. Both “HREE-rich”
552 cumulates, and LREE-rich melts may thus ultimately form economically viable REE deposits.

553

554 **Acknowledgments**

555 We thank C. Beard, P. Ulmer, D. Weidendorfer, and 2 anonymous reviewers for their useful
556 comments. We also thank the Tanzania commission for science and technology (COSTECH)
557 for the field permits. The authors acknowledge the help of Robert Dennen for English editing.
558 This research was financially supported by the French National Research Agency through the
559 national program “Investissements d'avenir” with the reference ANR-10-LABX-21
560 01/LABEX RESSOURCES21, and through the project GECO-REE (ANR-16-CE01-0003-01;
561 P.I.: Lydéric France). This study has also been supported by the Région Lorraine, and Région
562 Grand-Est, and PNP and CESSUR programs from INSU-CNRS (grants to Lydéric France).
563 This is CRPG contribution n° XX, and GECO-REE contribution n°XX.

564

565

566 **Figure captions**

567

568 **Fig. 1.** (a) Photomicrograph of clinopyroxenes hosted melt inclusions (reflected light) and (b)
569 (c) (d) BSE images from Oldoinyo Lengai melt inclusions. For the image (d), a small
570 “lighter” Cpx area is present which correspond to small chemical variation (dashed line). The
571 melt inclusions are likely CO₂-rich (deMoor et al. 2013) accounting for the large shrinkage
572 bubbles that are present; those presently containing residual polishing material. Major and
573 trace elements analyses of Cpx have been performed close to the melt inclusions. Numbers
574 correspond to the analyses reported in Table S1 & S2. Scale bars correspond to 10 μm.

575

576 **Fig. 2.** (a) Wollastonite (Wo)-Enstatite (En)-Ferrossilite (Fs) ternary diagram illustrating the
577 chemical variability of clinopyroxenes from various alkaline complexes. (b) Classification of
578 pyroxenes determined by Ca-Mg-Fe (Q = Wo-En-Fs), aegirine (Aeg) and jadeite (Jd)
579 components. (c) expanded Q-Aeg-Jd diagram (b) with Q > 80% (Morimoto 1988).
580 Clinopyroxene data are from Oldoinyo Lengai, Tanzania (this study, data used to calculate
581 D), Hanang volcano, Tanzania (Baudouin et al. 2016), Cape Verde (Weidendorfer et al.
582 2016), Gronnedal-Ika, Greenland (Marks et al. 2004), Ditrău, Romania (Bakti et al. 2018)
583 and from partition coefficient studies (natural samples: Mollo et al. 2016, Olin and Wolff
584 2010 and experimental studies: Beard et al. 2019, Hill et al. 2000, 2011; Dalou et al. 2012,
585 Adam and Green 2006).

586

587 **Fig. 3.** Cpx mineral chemistry. (a) Na vs Mg and (b) Fe³⁺ vs Al^{IV}; p.f.u. = per formula unit,
588 calculated for six oxygens. Fe³⁺ content of Cpx has been determined following the method of
589 Droop (1987). Cpx data are from Oldoinyo Lengai (this study), Hanang volcano, Tanzania
590 (Baudouin et al. 2016), Campi Flegrei, Italy, (Mollo et al., 2016), Ditrău, Romania (Bakti et
591 al. 2018), Cape Verde (Weidendorfer et al., 2016), Tenerife (Olin and Wolff 2010),
592 Gronnedal-Ika, Greenland (Marks et al. 2004) and experimental studies: Beard et al. 2019,
593 Hill et al. 2000, 2011; Dalou et al. 2012, Adam and Green 2006).

594

595 **Fig. 4.** Trace element variation diagrams for clinopyroxenes. (a) REE concentrations
596 normalized to chondrite and (b) extended trace element concentrations normalized to the
597 primitive mantle for diopside (Oldoinyo Lengai, this study; Baudouin et al., 2016; Campi
598 Flegrei, Mollo et al., 2016; Tenerife; Olin and Wolff 2010; Cape Verde; Weidendorfer et al.,

599 2016) and aegirine (Gronnedal-Ika, Marks et al., 2004). Normalization values are from
600 McDonough and Sun (1995).

601

602 **Fig. 5.** Major element composition of Cpx-hosted melt inclusions studied herein (10TL01
603 ijolite sample, (a) alkali vs SiO₂, (b) FeO vs SiO₂, (c) K₂O vs SiO₂, and (d) CaO vs SiO₂. Melt
604 composition from Beard et al. (2019), Mollo et al. (2016), Olin and Wolff (2010), Hill et al.
605 (2000), Dalou et al. (2012) and Adam & Green (2006) are also reported for comparison.

606

607

608 **Fig. 6.** Trace element partition coefficients ($D^{\text{Cpx/melt}}$) obtained in this study (alkali-rich
609 phonolite, Oldoinyo Lengai) and previous studies (experimental studies: Beard et al. 2019,
610 Adam and Green, 2006; Dalou et al., 2012; Hill et al., 2000, 2011; and natural samples: Mollo
611 et al., 2016; Olin and Wolff, 2010). Elements are ranked according to cation charge and
612 increasing ionic radius.

613

614 **Fig. 7.** (a) Zr/Nd vs Lu/Ho ratios in Cpx normalized to the primitive mantle (n subscript). (b)
615 Partition coefficient ratios between Zr and Nd vs Lu and Ho, highlighting the anomalous
616 distribution of HREE and HFSE compared to MREE between Cpx and phonolite melts.

617

618 **Fig. 8.** Lattice Strain model best fit to Oldoinyo Lengai Cpx. Red circles represent measured
619 $D^{\text{Cpx/phonolite melt}}$ values (error bars show 1σ uncertainties), and red and blue lines represent fits
620 for the M1 and M2 sites. Ionic radii are from Shannon (1976). The fit to data from Hill et al.
621 (2000) is also reported for comparison (open diamonds, dashed and dotted black lines
622 represent the M1 and M2 site best fits).

623

624 **Fig. 9.** Effect of Cpx chemistry on the ideal ionic radii for trivalent cations (r_0^{3+}) in the M1
625 site: (a) Mg and (b) Fe³⁺ contents per formula unit (p.f.u.). Symbols color code represents the
626 measured parameter $\text{Lu}^* (\%) = [D_{\text{Lu}}^{\text{M1}} / (D_{\text{Lu}}^{\text{M1}} + D_{\text{Lu}}^{\text{M2}})] \times 100$. Data presented here are from this
627 study (Oldoinyo Lengai, with black circles), Adam and Green (2006); Baudouin and Parat
628 (2015); Dalou et al. (2012); Hill et al. (2000); Mollo et al. (2016) and Olin and Wolff (2010).

629

630 **Fig. 10.** Parameters controlling HFSE partition coefficients: (a) D_{Ti} vs Al^{IV} (p.f.u.), (b) D_{Ti} vs
631 D_{Zr} , (c) D_{Ta} vs Al^{IV}, and (d) D_{Hf} vs D_{Zr} . Open squares present data compiled in Wood and
632 Blundy (2007) for basaltic melts. Red circles present data from this study, compiled in Table

633 S3 and green triangles are data from Mollo et al. (2016, Table S3) and diamonds are data from
634 Beard et al. 2019 (light blue diamonds: experimental data; dark blue diamonds: Canary
635 Islands data). Curves represent the best fits for phonolite melts in red (modeled from
636 equations presented in the equations 8 to 11) and for basaltic melts in black (modeled from
637 Wood and Blundy, 2007).

638
639

640 Fig. 11. Lattice strain model curves for DREE in six-fold (M1 site, red curve) and eight-fold
641 (M2 site, blue curve) coordination, and the sum of the two curves (black curve). Red circles
642 represent measured $D^{\text{Cpx/phonolitic melt}}$ values. DREE for each sites are calculated by using the
643 equations described in the text section “Calculation of the strain energy (ΔG)”.

644

645 **Fig. 12.** Lu/Ho ratio in Cpx normalized to the primitive mantle (n subscript) vs Lu* calculated
646 from the major element content of Cpx (equation 3). No melt data are available for the Cpx
647 presented here. The color scale shows the Fe^{3+} content in Cpx varying from 0 to 0.3 p.f.u. Cpx
648 data are from Bakti et al. (2018), Baudouin and Parat (2015), Baudouin et al. (2016), Marks et
649 al. (2004), Möller and Williams-Jones, (2016), Vuorinen et al. (2005), and Weidendorfer et al.
650 (2016). Normalization values are from McDonough and Sun (1995).

651

652 **Fig. 13.** REE partition coefficients vs ionic radii. Measured partition coefficients (red circles)
653 and those calculated in this study (OL= Oldoinyo Lengai sample, open circles) are in good
654 agreement, especially for HREE (Er, Tm, Yb, Lu). Calculated partition coefficients from the
655 lattice strain model using parameters derived from Beard et al. (2019, blue diamonds); Mollo
656 et al. (2016, green triangles) and Wood and Blundy (1997, black diamonds) fail to reproduce
657 the Cpx-alkaline melt HREE partition coefficients studied herein.

658

659 Fig. 14. REE evolution of phonolitic melt through fractional crystallization
660 (%crystallization=85%). Evolved melt (full lines) and cumulates (dotted lines) are calculated
661 by using partition coefficients calibrated for basalt (A. & G. 2006: Adam and Green 2006)
662 and for phonolite (this study) to highlight the importance of using the accurate partition
663 coefficient values if we are to quantify melt and cumulate REE contents. Presented models
664 highlight that REE contents similar to natural carbonatites can be obtained (Bayan Obo
665 carbonatites, Yang et al. 2000; Alnö carbonatites, Hornig-Kjarsgaard 1998). We also report
666 crystallization model including 10% of wollastonite (partition coefficient from B. & F. 2019:

667 Baudouin and France 2019). Crystallization of accessory minerals such as wollastonite (as
668 well apatite, titanite) have a potential strong impact on REE distribution between melt and
669 cumulates and should thus be considered.

670

671

672

673

674 References

675

676 Adam J, Green T (2006) Trace element partitioning between mica-and amphibole-bearing
677 garnet lherzolite and hydrous basanitic melt: 1. Experimental results and the investigation
678 of controls on partitioning behaviour. *Contrib. Mineral. Petrol.* 152(1), 1-17.

679 Batki A, Pál-Molnár E, Jankovics MÉ, Kerr AC, Kiss B, Markl G, Heincz A, Harangi S
680 (2018) Insights into the evolution of an alkaline magmatic system: An in situ trace element
681 study of clinopyroxenes from the Ditrău Alkaline Massif, Romania. *Lithos*, 300, 51-71.
682 <https://doi.org/10.1016/j.lithos.2017.11.029>

683 Baudouin C, France L (2019) Trace element partitioning between wollastonite and alkaline
684 silicate magmas. *Chemical Geology*, 523, 88-94.

685 Baudouin C, Parat F (2015) Role of volatiles (S, Cl, H₂O) and silica activity on the
686 crystallization of hauyne and nosean in phonolitic magmas (Eifel, Germany and Saghro,
687 Morocco). *American Mineralogist*, 100(10), 2308-2322. <https://doi.org/10.2138/am-2015-5318>
688

689 Baudouin C, Parat F, Denis CM, Mangasini F (2016) Nephelinite lavas at early stage of rift
690 initiation (Hanang volcano, North Tanzanian Divergence). *Contrib. Mineral. Petrol.*
691 171(7), 64. doi: [10.1007/s00410-016-1273-5](https://doi.org/10.1007/s00410-016-1273-5)

692 Beard, CD, van Hinsberg, VJ, Stix, J, Wilke, M (2019) Clinopyroxene/melt trace element
693 partitioning in sodic alkaline magmas. *Journal of Petrology*.

694 Bédard JH (2014) Parameterizations of calcic clinopyroxene—Melt trace element partition
695 coefficients. *Geochemistry, Geophysics, Geosystems*, 15(2), 303-336.

696 Bennett SL, Blundy J, Elliott T (2004) The effect of sodium and titanium on crystal-melt
697 partitioning of trace elements. *Geochimica et Cosmochimica Acta*, 68(10), 2335-2347.
698 <https://doi.org/10.1016/j.gca.2003.11.006>

699 Blundy J, Wood B (1994) Prediction of crystal–melt partition coefficients from elastic
700 moduli. *Nature*, 372(6505), 452.

701 Blundy J, Wood B (2003) Partitioning of trace elements between crystals and melts. *Earth and*
702 *Planetary Science Letters*, 210(3-4), 383-397. [https://doi.org/10.1016/S0012-821X\(03\)00129-8](https://doi.org/10.1016/S0012-821X(03)00129-8)
703

704 Blundy JD, Robinson JAC, Wood BJ (1998) Heavy REE are compatible in clinopyroxene on
705 the spinel lherzolite solidus. *Earth and Planetary Science Letters*, 160(3), 493-504.
706 [https://doi.org/10.1016/S0012-821X\(98\)00106-X](https://doi.org/10.1016/S0012-821X(98)00106-X)

707 Bottazzi P, Tiepolo M, Vannucci R, Zanetti A, Brumm R, Foley SF, Oberti R (1999) Distinct
708 site preferences for heavy and light REE in amphibole and the prediction of Amph/L D
709 REE. *Contrib. Mineral. Petrol.* 137(1-2), 36-45.

710 Braunger, S., Marks, M. A. W., Walter, B. F., Neubauer, R., Reich, R., Wenzel, T., Markl, G.
711 (2018) The petrology of the Kaiserstuhl Volcanic Complex, SW Germany: the importance of
712 metasomatized and oxidized lithospheric mantle for carbonatite generation. *Journal of*
713 *Petrology*, 59(9), 1731-1762.

714

- 715 Brice JC (1975) Some thermodynamic aspects of the growth of strained crystals. *Journal of*
716 *Crystal Growth*, 28(2), 249-253. [https://doi.org/10.1016/0022-0248\(75\)90241-9](https://doi.org/10.1016/0022-0248(75)90241-9)
- 717 Cameron M, Papike JJ (1980) Crystal chemistry of silicate pyroxenes. *Reviews in Mineralogy*
718 *and Geochemistry*, 7(1), 5-92.
- 719 Dalou C, Koga KT, Shimizu N, Boulon J, Devidal JL (2012) Experimental determination of F
720 and Cl partitioning between lherzolite and basaltic melt. *Contrib. Mineral. Petrol.* 163(4),
721 591-609. doi: [10.1007/s00410-011-0688-2](https://doi.org/10.1007/s00410-011-0688-2)
- 722 Dalou C, Boulon J, Koga KT, Dalou R, Dennen R (2018). DOUBLE FIT: Optimization
723 procedure applied to lattice strain model. *Computers & Geosciences*, 117, 49-56.
- 724 Dawson JB (1998) Peralkaline nephelinite–natrocarbonatite relationships at Oldoinyo Lengai,
725 Tanzania. *Journal of Petrology*, 39(11-12), 2077-2094.
726 <https://doi.org/10.1093/петroj/39.11-12.2077>
- 727 de Moor JM, Fischer TP, King PL, Botcharnikov RE, Hervig RL, Hilton DR, Ramirez C
728 (2013). Volatile-rich silicate melts from Oldoinyo Lengai volcano (Tanzania): Implications
729 for carbonatite genesis and eruptive behavior. *Earth and Planetary Science Letters*, 361,
730 379-390.
- 731 Droop GTR (1987). A general equation for estimating Fe³⁺ concentrations in ferromagnesian
732 silicates and oxides from microprobe analyses, using stoichiometric criteria. *Mineralogical*
733 *magazine*, 51(361), 431-435.
- 734 Dygert N, Liang Y, Sun C, Hess P (2014) An experimental study of trace element partitioning
735 between augite and Fe-rich basalts. *Geochimica et Cosmochimica Acta*, 132, 170-186.
736 <https://doi.org/10.1016/j.gca.2014.01.042>
- 737 Fedele L, Zanetti A, Morra V, Lustrino M, Melluso L, Vannucci R (2009)
738 Clinopyroxene/liquid trace element partitioning in natural trachyte–trachyphonolite
739 systems: insights from Campi Flegrei (southern Italy). *Contrib. Mineral. Petrol.* 158(3),
740 337-356. doi: [10.1007/s00410-009-0386-5](https://doi.org/10.1007/s00410-009-0386-5)
- 741 Gaetani GA (2004) The influence of melt structure on trace element partitioning near the
742 peridotite solidus. *Contrib. Mineral. Petrol.* 147(5), 511-527.
- 743 Gaetani GA, Grove TL (1995) Partitioning of rare earth elements between clinopyroxene and
744 silicate melt crystal-chemical controls. *Geochimica et Cosmochimica Acta*, 59(10), 1951-
745 1962. [https://doi.org/10.1016/0016-7037\(95\)00119-0](https://doi.org/10.1016/0016-7037(95)00119-0)
- 746 Griffin WL, Powell W, Pearson NJ, O'Reilly SY (2008) GLITTER: data reduction software
747 for laser ablation ICP–MS. *Laser Ablation–ICP–MS in the Earth Sciences* vol. 40.
748 Mineralogical Association of Canada Short Course Series, pp. 204-207
- 749 Hill E, Wood BJ, Blundy JD (2000) The effect of Ca-Tschermaks component on trace
750 element partitioning between clinopyroxene and silicate melt. *Lithos*, 53(3), 203-215.
751 [https://doi.org/10.1016/S0024-4937\(00\)00025-6](https://doi.org/10.1016/S0024-4937(00)00025-6)
- 752 Hill E, Blundy JD, Wood BJ (2011) Clinopyroxene–melt trace element partitioning and the
753 development of a predictive model for HFSE and Sc. *Contrib. Mineral. Petrol.* 161(3), 423-
754 438. doi: [10.1007/s00410-010-0540-0](https://doi.org/10.1007/s00410-010-0540-0)

- 755 Hornig-Kjarsgaard, I. (1998) Rare earth elements in sövitic carbonatites and their mineral
756 phases. *Journal of Petrology*, 39(11-12), 2105-2121.
757
- 758 Huang F, Lundstrom CC, McDonough WF (2006) Effect of melt structure on trace-element
759 partitioning between clinopyroxene and silicic, alkaline, aluminous melts. *American*
760 *Mineralogist*, 91(8-9), 1385-1400. <https://doi.org/10.2138/am.2006.1909>
- 761 Keller J, Krafft M (1990) Effusive natrocarbonatite activity of Oldoinyo Lengai, June 1988.
762 *Bulletin of Volcanology*, 52(8), 629-645.
- 763 Lundstrom CC, Shaw HF, Ryerson FJ, Phinney DL, Gill JB, Williams Q (1994)
764 Compositional controls on the partitioning of U, Th, Ba, Pb, Sr and Zr between
765 clinopyroxene and haplobasaltic melts: implications for uranium series disequilibria in
766 basalts. *Earth and Planetary Science Letters*, 128(3-4), 407-423.
- 767 McDonough WF, Sun SS (1995). The composition of the Earth. *Chemical geology*, 120(3-4),
768 223-253.
- 769 Masotta M, Mollo S, Freda C, Gaeta M, Moore G (2013) Clinopyroxene–liquid thermometers
770 and barometers specific to alkaline differentiated magmas. *Contributions to Mineralogy*
771 *and Petrology* 166(6), 1545-1561. <http://doi.org/10.1007/s00410-013-0927-9>
- 772 Marks M, Halama R, Wenzel T, Markl G (2004) Trace element variations in clinopyroxene
773 and amphibole from alkaline to peralkaline syenites and granites: implications for mineral–
774 melt trace-element partitioning. *Chemical geology*, 211(3), 185-215.
775 <https://doi.org/10.1016/j.chemgeo.2004.06.032>
- 776 Martin LH, Schmidt MW, Mattsson HB, Guenther D (2013) Element partitioning between
777 immiscible carbonatite and silicate melts for dry and H₂O-bearing systems at 1–3 GPa.
778 *Journal of Petrology*, 54(11), 2301-2338.
- 779 Michely LT, Leitzke FP, Speelmanns IM, Fonseca ROC (2017) Competing effects of crystal
780 chemistry and silicate melt composition on trace element behavior in magmatic systems:
781 insights from crystal/silicate melt partitioning of the REE, HFSE, Sn, In, Ga, Ba, Pt and
782 Rh. *Contributions to Mineralogy and Petrology*, 172(6), 39.
- 783 Möller V, Williams-Jones AE (2016) Petrogenesis of the Nechalacho Layered Suite, Canada:
784 magmatic evolution of a REE–Nb-rich nepheline syenite intrusion. *Journal of Petrology*,
785 57(2), 229-276. <https://doi.org/10.1093/petrology/egw003>
- 786 Mollex G, Furi E, Burnard P, Zimmermann L, Chazot G, Kazimoto EO, Marty B, France L
787 (2018) Tracing helium isotope compositions from mantle source to fumaroles at Oldoinyo
788 Lengai volcano, Tanzania. *Chemical Geology* 480(5), 66-74.
- 789 Mollex G (2017) Architecture de la plomberie du volcan carbonatitique Oldoinyo Lengai:
790 nouvelles contraintes sur la source, les transferts hydrothermaux, et la différenciation
791 magmatique dans la chambre active (PhD thesis, Université de Lorraine)
- 792 Mollo S, Putirka K, Misiti V, Soligo M, Scarlato P (2013) A new test for equilibrium based
793 on clinopyroxene-melt pairs: Clues on the solidification temperatures of Etnean alkaline
794 melts at post eruptive conditions. *Chemical Geology* 352, 92–100.
795 <http://dx.doi.org/10.1016/j.chemgeo.2013.05.026>

- 796 Mollo S, Forni F, Bachmann O, Blundy JD, De Astis G, Scarlato P (2016) Trace element
797 partitioning between clinopyroxene and trachy-phonolitic melts: A case study from the
798 Campanian Ignimbrite (Campi Flegrei, Italy). *Lithos*, 252, 160-172.
799 <https://doi.org/10.1016/j.lithos.2016.02.024>
- 800 Mollo S, Blundy J, Scarlato P, De Cristofaro SP, Tecchiato V, Di Stefano F, Vetere
801 Bachmann O (2018) An integrated P-T-H₂O-lattice strain model to quantify the role of
802 clinopyroxene fractionation on REE+ Y and HFSE patterns of mafic alkaline magmas:
803 Application to eruptions at Mt. Etna. *Earth-Science Reviews*, 185, 32-56.
- 804 Morimoto N (1988) Nomenclature of pyroxenes. *Mineralogy and Petrology*, 39(1), 55-76.
- 805 Nagasawa H (1966) Trace element partition coefficient in ionic crystals. *Science*, 152(3723),
806 767-769.
- 807 Olin PH, Wolff JA (2010) Rare earth and high field strength element partitioning between
808 iron-rich clinopyroxenes and felsic liquids. *Contrib. Mineral. Petrol.* 160(5), 761-775.
809 doi: [10.1007/s00410-010-0506-2](https://doi.org/10.1007/s00410-010-0506-2)
- 810 Onuma N, Higuchi H, Wakita H, Nagasawa H (1968) Trace element partition between two
811 pyroxenes and the host lava. *Earth and Planetary Science Letters*, 5, 47-51.
812 [https://doi.org/10.1016/S0012-821X\(68\)80010-X](https://doi.org/10.1016/S0012-821X(68)80010-X)
- 813 Reguir EP, Chakhmouradian AR, Pisiak L, Halden NM, Yang P, Xu C, Kynicky J, Couëslan
814 CG (2012) Trace-element composition and zoning in clinopyroxene-and amphibole-group
815 minerals: implications for element partitioning and evolution of carbonatites. *Lithos*, 128,
816 27-45. <https://doi.org/10.1016/j.lithos.2011.10.003>
- 817 Shannon RD (1976) Revised effective ionic radii and systematic studies of interatomic
818 distances in halides and chalcogenides. *Acta crystallographica section A: crystal physics,*
819 *diffraction, theoretical and general crystallography*, 32(5), 751-767.
- 820 Vuorinen JH, Hålenius U, Whitehouse MJ, Mansfeld J, Skelton AD (2005) Compositional
821 variations (major and trace elements) of clinopyroxene and Ti-andradite from pyroxenite,
822 ijolite and nepheline syenite, Alnö Island, Sweden. *Lithos*, 81(1-4), 55-77.
823 <https://doi.org/10.1016/j.lithos.2004.09.021>
- 824 Weidendorfer D, Schmidt MW, Mattsson HB (2016) Fractional crystallization of Si-
825 undersaturated alkaline magmas leading to unmixing of carbonatites on Brava Island (Cape
826 Verde) and a general model of carbonatite genesis in alkaline magma suites. *Contrib.*
827 *Mineral. Petrol.* 171(5), 43. doi: [10.1007/s00410-016-1249-5](https://doi.org/10.1007/s00410-016-1249-5)
- 828 Wood BJ, Blundy JD (2001) The effect of cation charge on crystal–melt partitioning of trace
829 elements. *Earth and Planetary Science Letters*, 188(1-2), 59-71.
- 830 Wood BJ, Blundy JD (1997) A predictive model for rare earth element partitioning between
831 clinopyroxene and anhydrous silicate melt. *Contrib. Mineral. Petrol.* 129(2-3), 166-181.
- 832 Wood BJ, Blundy JD (2007) Trace element partitioning under crustal and uppermost mantle
833 conditions: the influences of ionic radius, cation charge, pressure, and temperature.
834 *Treatise on Geochemistry*, 2, 568.

- 835 Woodland AB, Jugo PJ (2007). A complex magmatic system beneath the Deves volcanic
836 field, Massif Central, France: evidence from clinopyroxene megacrysts. *Contributions to*
837 *Mineralogy and Petrology*, 153(6), 719-731.
838
- 839 Yang, X. M., Yang, X. Y., Chen, T. H., Zhang, P. S., Tao, K. J., Le Bas, M. J., Henderson, P.
840 (2000) Geochemical characteristics of a carbonatite dyke rich in rare earths from Bayan Obo,
841 China.
842
- 843 Zhang C, Koepke J, France L, Godard M (2017) Felsic Plutonic Rocks from IODP Hole
844 1256D, Eastern Pacific: Implications for the Nature of the Axial Melt Lens at Fast-
845 Spreading Mid-Ocean Ridges. *Journal of Petrology*, 58(8), 1535-1565. doi:
846 10.1093/petrology/egx064

847 Tables
848

Table 1. Partition coefficients (D)
between Cpx and phonolite melt.

	D	σ
Rb	0.0001	0.00003
Ba	0.0002	0.0001
Li	0.80	0.2
Th	0.0003	0.0001
Ta	0.0016	0.001
Nb	0.0003	0.0001
La	0.013	0.005
Ce	0.018	0.0076
Pr	0.029	0.011
Sr	0.659	0.233
Nd	0.041	0.01
Hf	0.247	0.10
Zr	0.134	0.06
Sm	0.062	0.02
Eu	0.062	0.01
Gd	0.063	0.02
Ti	0.314	0.16
Tb	0.064	0.02
Dy	0.056	0.01
Ho	0.063	0.02
Er	0.074	0.03
Tm	0.122	0.05
Yb	0.219	0.09
Lu	0.412	0.14
Sc	1.092	0.39
V	0.627	0.33
Ge	0.824	0.49
Al	0.034	0.01
Na	0.165	0.02
Mn	1.152	0.52
K	0.002	0.001

849

850

Table 2. Lattice strain parameters for trivalent and tetravalent cations (Cpx-phonolite, Oldoinyo Lengai).

	M1 site				M2 site			
	mean	σ	min	max	mean	σ	min	max
D_0^{3+}	1.240	0.441	0.62	1.92	0.07	0.015	0.05	0.09
E^{3+}	382	48	295	459	390	34	325	441
r_0^{3+}	0.740	0.006	0.73	0.75	1.05	0.017	1.01	1.07
D_0^{4+}	0.896	0.116	0.73	1.08				
E^{4+}	2071	213	1736	2397				
r_0^{4+}	0.658	0.002	0.655	0.662				

851

Fig 1

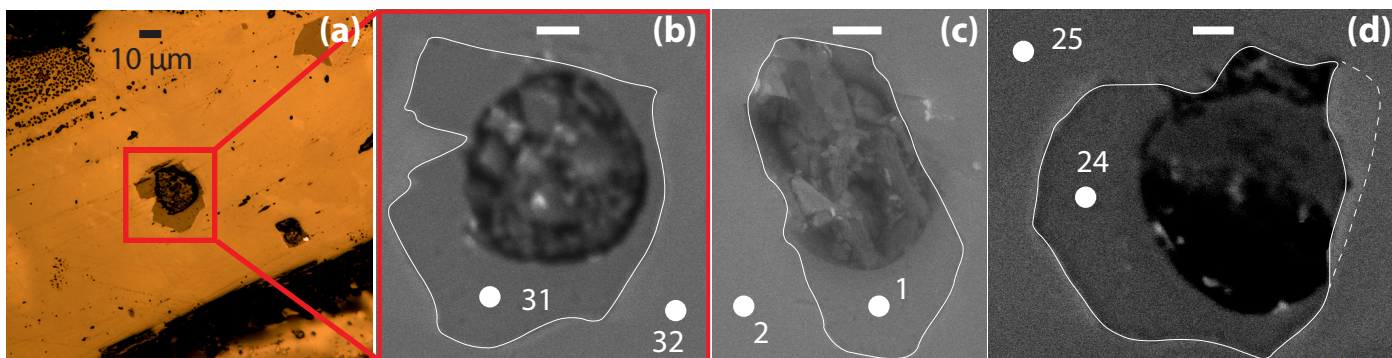


Fig 2

- ◆ Baudouin et al. 2016
· Weidendorfer et al. 2016
● Marks et al. 2004
● Bakti et al. 2018
- Studies with D provided
● Phonolite (this study)
▲ Mollo et al. 2016
× Olin and Wolff 2010
- From experimental studies:
◇ Hill et al. 2000, 2011
□ Dalou et al. 2012
○ Adam and Green 2006
◆ Beard et al. 2019

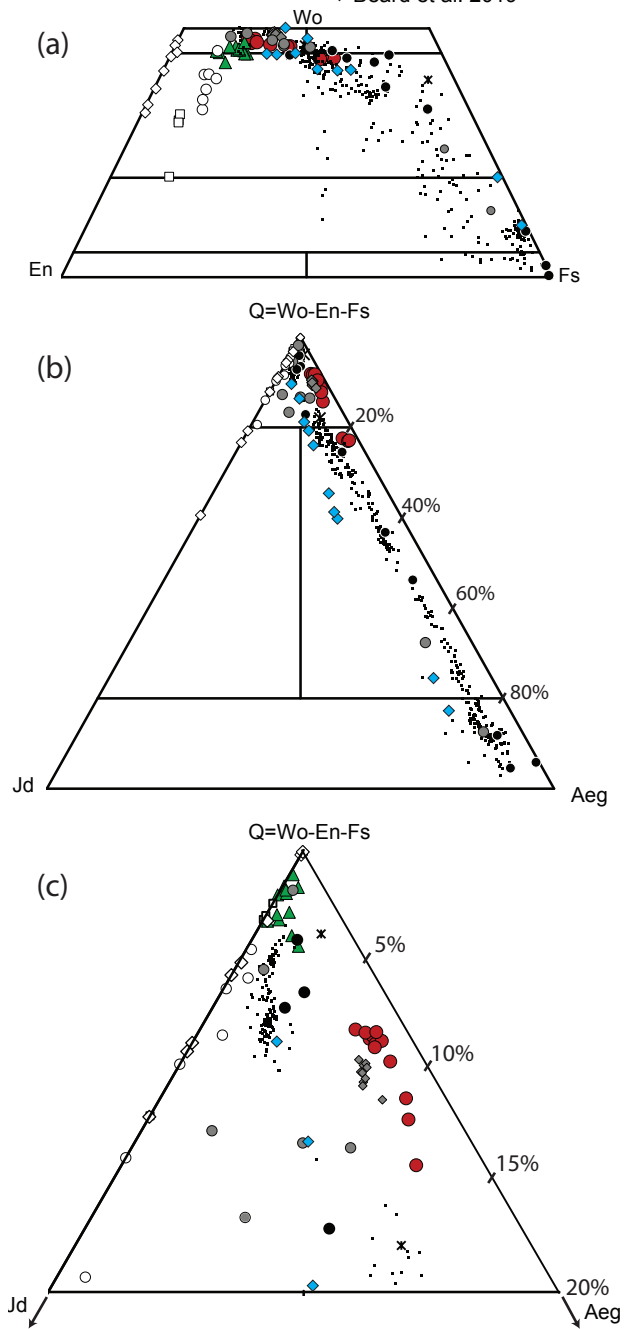


Fig 3

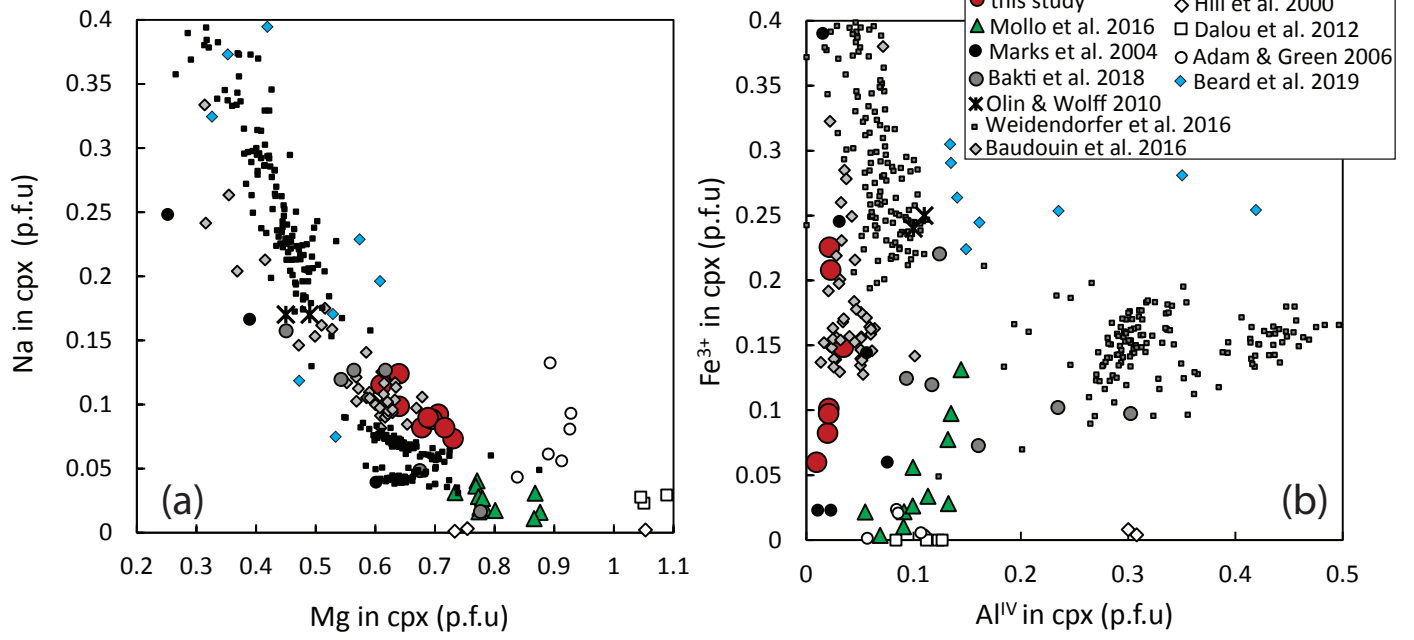


Fig 4

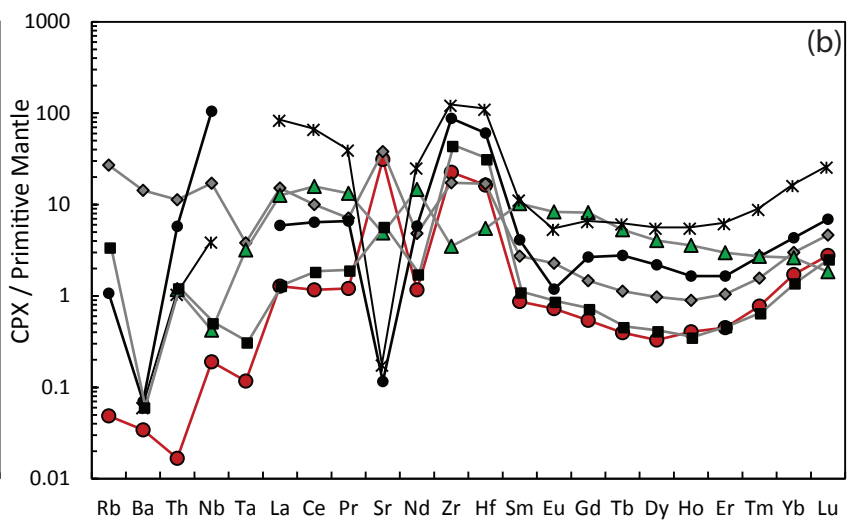
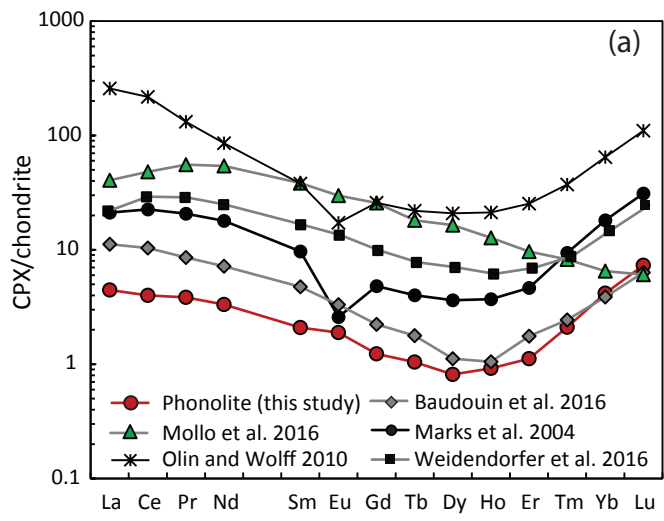


Fig 5

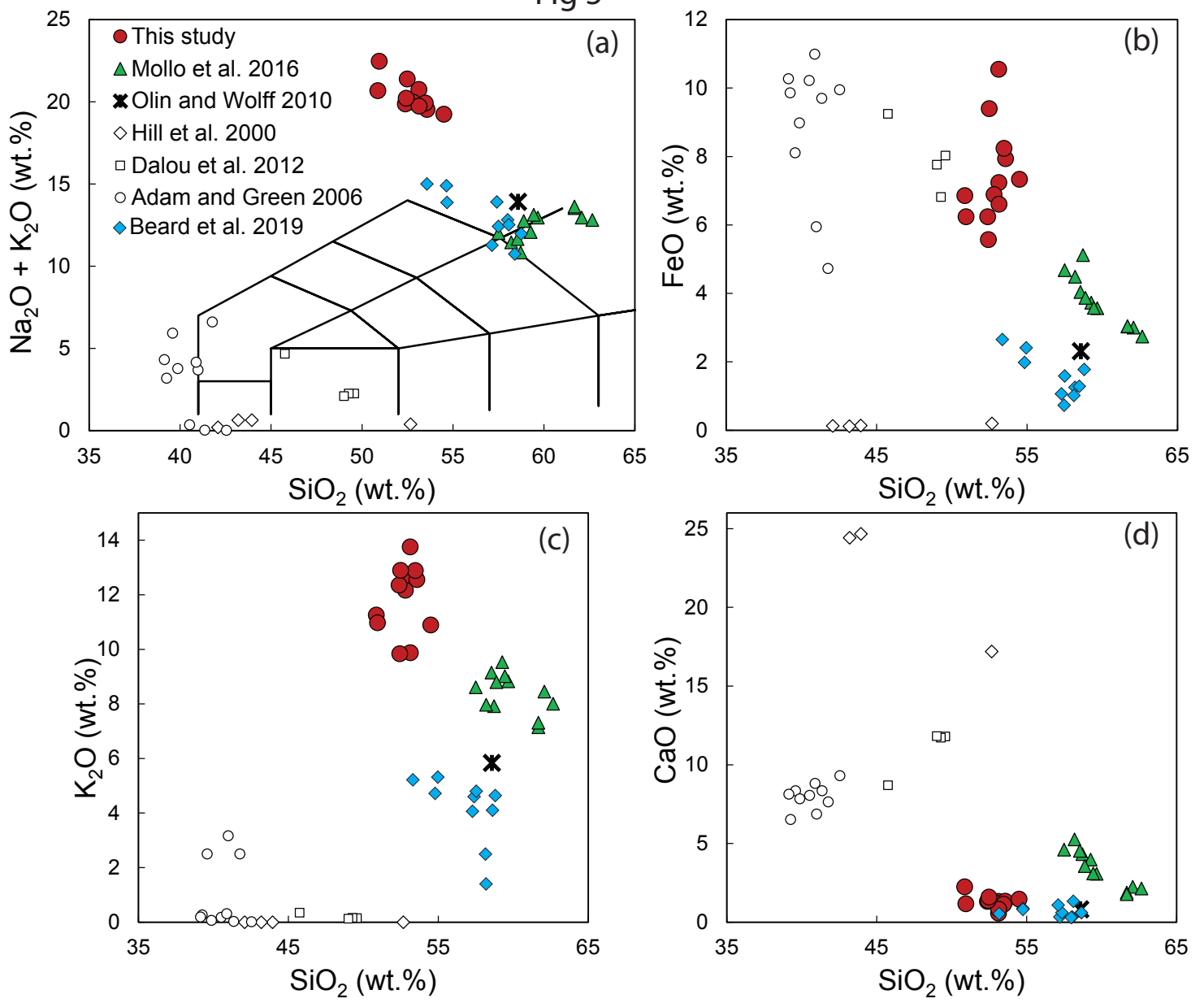


Fig 6

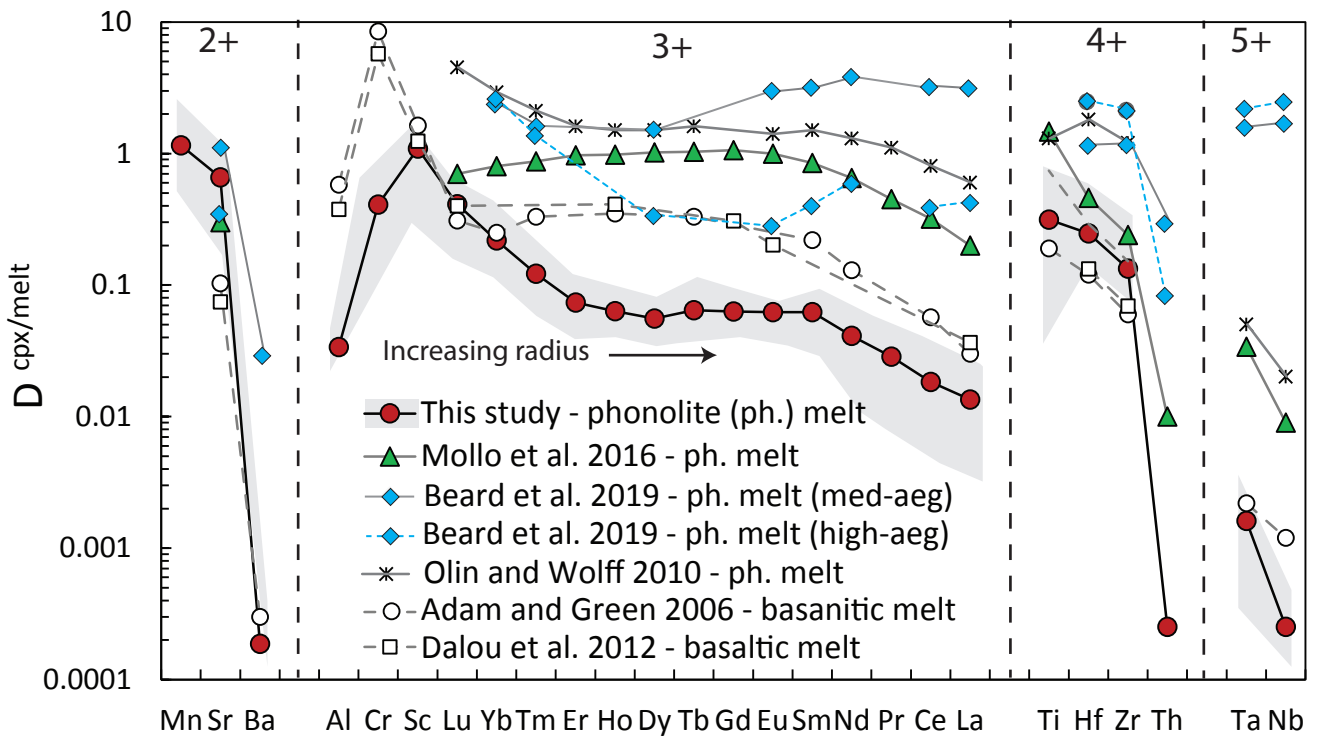


Fig 7

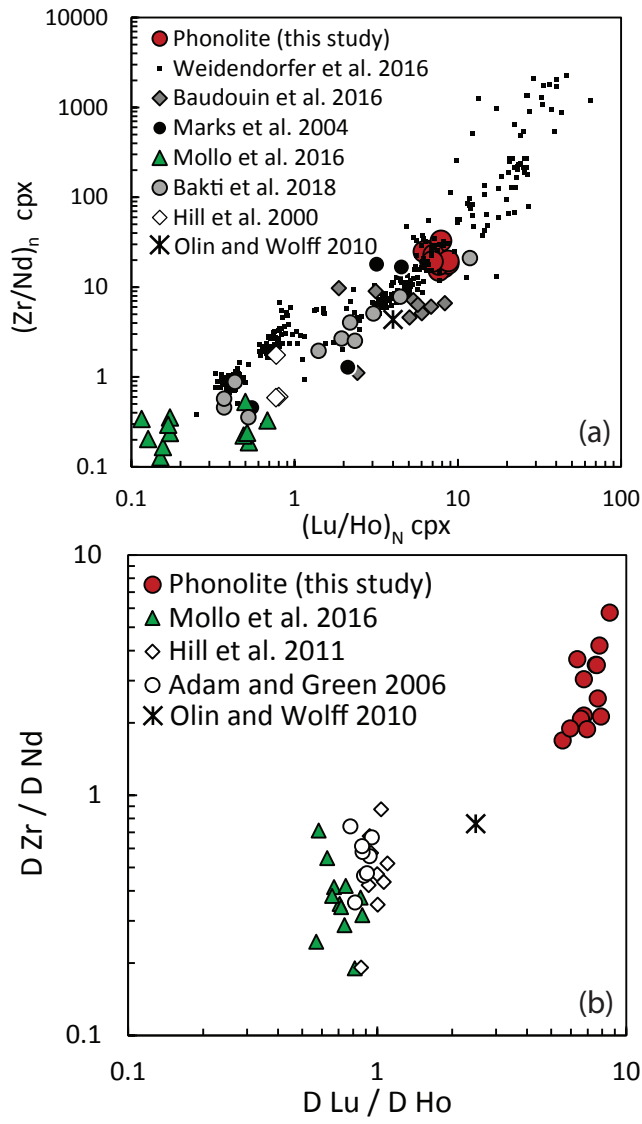


Fig 8

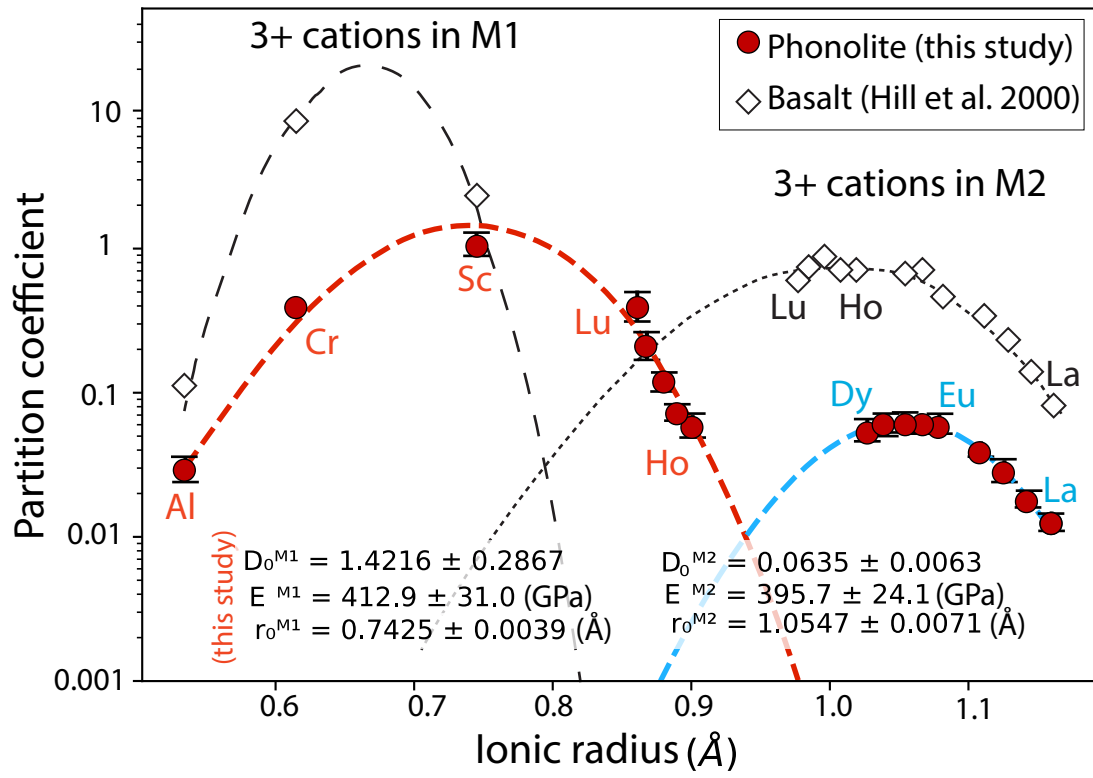


Fig 9

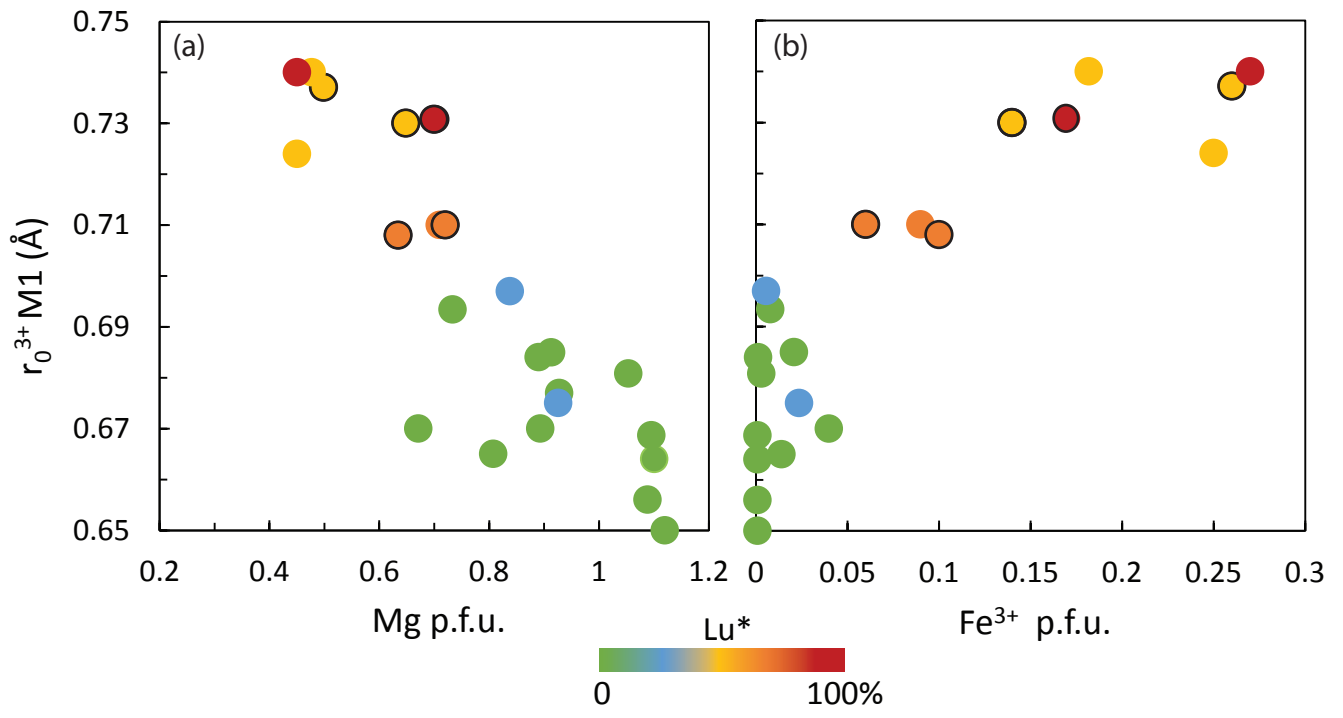


Fig 10

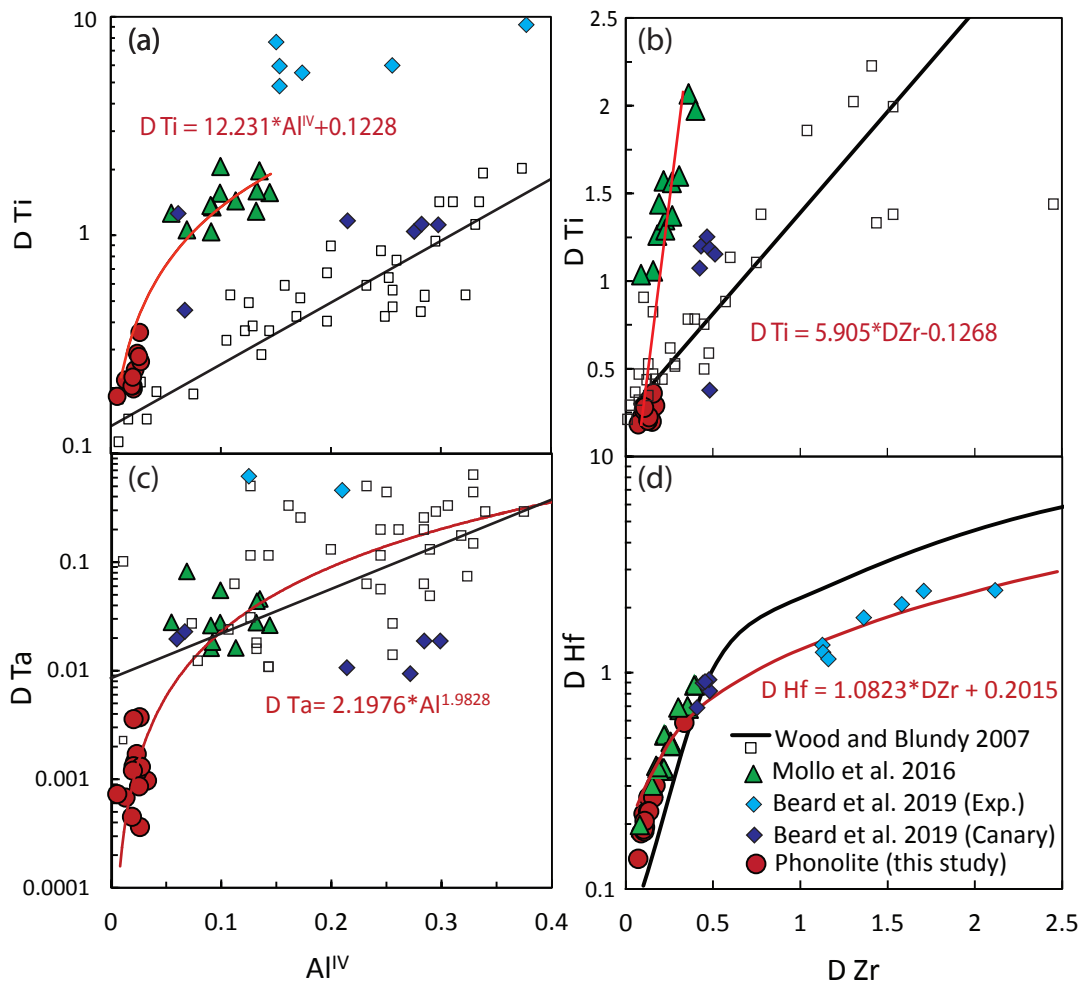


Figure 11

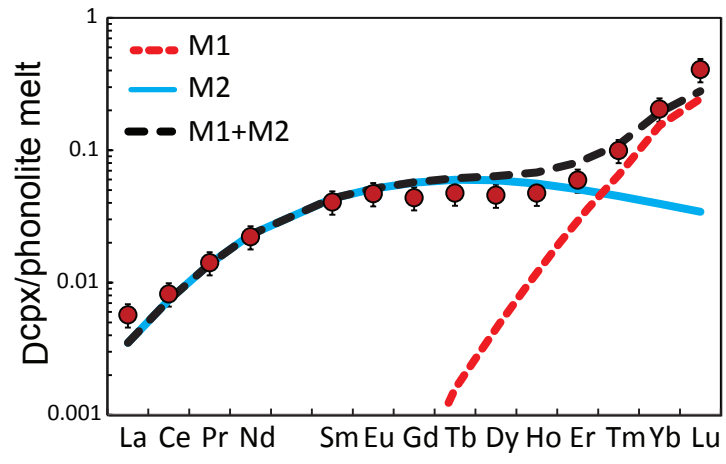


Fig 12

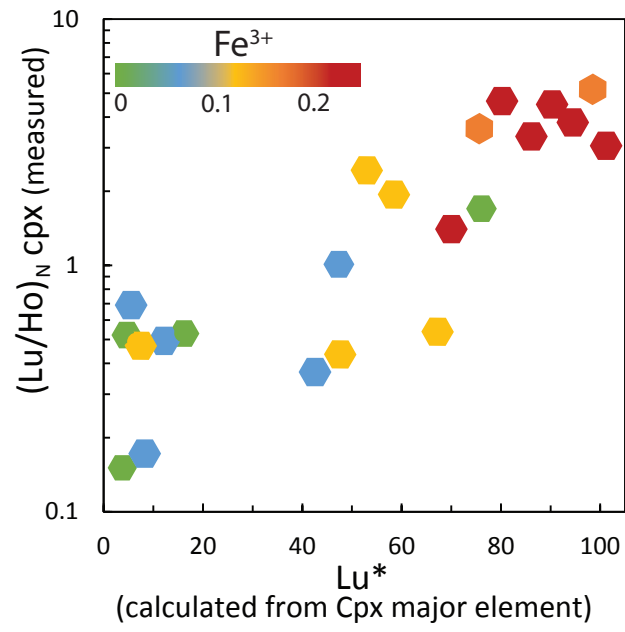


Fig 13

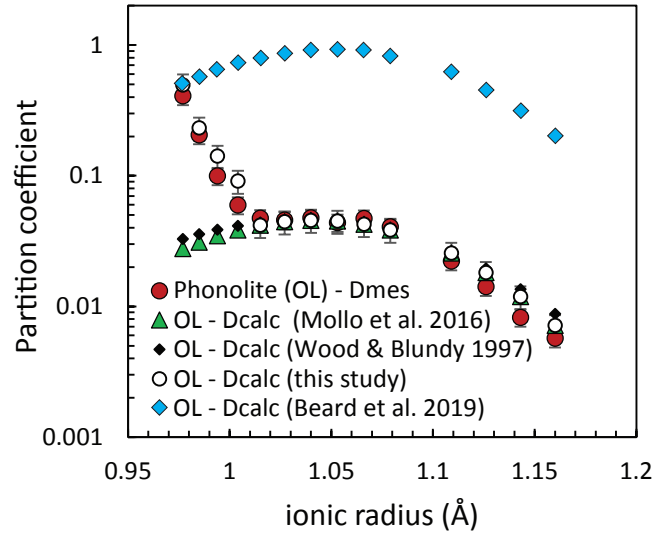


Figure 14

